Factors Governing Cloud Growth and Entrainment Rates in Shallow Cumulus and Cumulus Congestus During GoAmazon 2014/2015

By
Jordan M. Eissner

Submitted to the graduate degree program in Geography and Atmospheric Sciences and the Graduate Faculty of the University of Kansas in partial fulfillment of the requirements for the degree of Master of Science.

Chair: David B. Mechem

Michael P. Jensen

Justin Stachnik

Date Defended: 7/16/2020

The thesis committee for Jordan Eissner certifies that this is the approved version of the following thesis:

Factors Governing Cloud Growth and Entrainment Rates in Shallow Cumulus and Cumulus Congestus During GoAmazon 2014/2015

Co-Chair: David B. Mechem

Date Approved: 7/23/2020

Abstract

Shallow cumulus and cumulus congestus clouds play an important role in the large-scale tropical circulation by mixing heat and moisture vertically and preconditioning the environment for deeper convection. Different representations of these shallow clouds also account for much of the spread in General Circulation Models (GCMs) climate sensitivity. In particular, GCMs typically struggle representing low-cloud cover and the diurnal cycle in cloud properties. One of the reasons for these shortcomings may be how entrainment is represented in GCM parameterizations. Entrainment is a first-order mechanism that governs the depth to which shallow cumulus and congestus penetrate. This study uses observations from the Department of Energy's Atmospheric Radiation Measurement (ARM) mobile facility deployed at Manacapuru, Brazil during the Green Ocean Amazon (GOAmazon) 2014/2015 Campaign. Environmental thermodynamic profiles and observations of cloud-top height are used to constrain an entraining plume model to estimate bulk entrainment rates. A new and improved best-estimate of cloud-top height is obtained from a combination of vertically-pointing W-band ARM cloud radar (WACR) and 1290-MHz Radar Wind Profiler (RWP) observations. A combination of radiosonde, microwave radiometer profiler (MWRP) and microwave radiometer (MWR) observations provide a new and improved best-estimate of the environmental thermodynamic state. We quantify uncertainty in entrainment rates considering uncertainties in estimated cloud top height, environmental thermodynamic properties, and assumed initial parcel characteristics.

We evaluate several entrainment closures that are in current use in atmospheric models or have been proposed based on theory or large-eddy simulation results. Entrainment rates for cumulus congestus clouds are weakly correlated with low-level buoyancy, cloud depth, and cloud size. For shallow cumulus, we find a modest correlation between entrainment rate and low-

level relative humidity. Additional relationships between entrainment rate, vertical velocity, and environmental thermodynamic variables are also presented.

Acknowledgments

I would like to thank my advisor, Dr. David Mechem, for the countless hours spent giving me knowledge and guidance to complete my thesis. Also, thank you to my committee members, Dr. Justin Stachnik and Dr. Michael Jensen, for all of their assistance, time, and contributions to this research. Thank you to Dr. Scott Giangrande at Brookhaven National Laboratory for all of the advice regarding the instruments used in this study. This project would not have been possible without the support and funding (award number DE-SC0016522) from the Department of Energy. I also would like to acknowledge the DOE ARM Climate Research Facility for providing all of the data to do this study.

Thank you to all of the Department of Geography and Atmospheric Science faculty for the opportunity to learn and further my growth as a scientist. Thank you to my fellow atmospheric science graduate students, especially Brett Chrisler and Luke McMichael, for all of the meaningful discussions and friendship. And finally, I would like to thank my family, Jay, Rose Lee, and Gabriele Eissner, Gabriel Valencia, and the rest of my extended family and friends for believing in me and supporting me throughout my education.

Table of Contents

1 Introduction 1

2 Data 6

3 Methods 9

3.1 *Observational estimates of entrainment rate* 9

3.2 *Best estimate of CTH* 12

3.3 *Best estimate thermodynamic profile* 15

3.4 *Best estimate entrainment rates* 19

3.5 *Evaluating environmental controls on entrainment rates* 21

3.6 *Quantifying measurement uncertainty* 24

3.7 *Sensitivity tests* 27

4 Results 29

4.1 *Entrainment rates* 29

4.2 *Observational evaluation of entrainment closures in atmospheric models* 29

4.2.1 Linear regression 29

4.2.2 Regression Trees and Random Forests 38

4.3 *Uncertainty in entrainment rate calculations* 43

4.4 *Sensitivity tests* 44

5 Conclusions and Discussion 49

Appendix 54

Thermodynamic uncertainty estimates 54

References 55

List of Figures

Figure 1: The location of the GoAmazon2014/5 field campaign. The AMF is located at the red dot, site T3, 70 km west of the center of Manaus (Figure 1 from Giangrande et al. 2017)..... 8

Figure 2: The "entraining plume" model used to find the entrainment rate. The blue line represents the environmental θ_e. The black line is the undiluted parcel θ_e, and the red lines are the parcel θ_e experiencing different amounts of entrainment. Here, the entrainment rate is 0.15 km^{-1} since that is the rate at which the CTH equals the ELNB..... 11

Figure 3: The virtual temperature profiles of the environment and parcel. The parcel virtual temperature will never be less than the environment below CTH and thus an entrainment rate for this case cannot be calculated. 11

Figure 4: The WACR reflectivity and RWP echo classification for a congestus cloud on April 4th, 2014. The WACR is clearly attenuating due to the precipitation and does not sample the entire cloud. Therefore, we use the RWP-sampled CTH..... 13

Figure 5: The RWP CTH vs ARSCL CTH color-coded by the CTH difference. The red points indicate that the RWP is larger and the blue points indicate that the ARSCL CTH is larger. The horizontal black line represents the upper-limit of congestus clouds (9km) and the diagonal black line is the 1:1 line..... 13

Figure 6: A histogram of cloud top heights of all the clouds used in this study. Shallow have CTH < 3 km and congestus have CTH between 3 and 9 km..... 15

Figure 7: Vertical profiles of the radiosonde, MWRP at the time of the sounding and cloud and their difference, and corrected profile temperature (a) and mixing ratio (b)..... 17

Figure 8: A comparison of the MWRP thermodynamic best estimate to the sounding using stability variables: low- level CAPE (a), CIN (b), and mid-level ELR (c)..... 19

Figure 9: The ER calculated using ARSCL CTHs and best estimate thermodynamic profile versus the ER calculated from the best estimate CTH and thermodynamic profile, color-coded by the difference between the best estimate CTH and ARSCL CTH (a). The ER calculated using the sounding thermodynamic profiles and best estimate CTH versus the ER calculated from the best estimate CTH and thermodynamic profile, color-coded by the time difference between the cloud and sounding (b). The black line is the 1:1 line. 20

Figure 10: Idealized temperature and relative humidity profiles adapted from June 28, 2015 at 17:44Z (black) with the addition and subtraction of the instrumental uncertainty profiles and the magnitudes of the uncertainty in each level for temperature (a, red) and relative humidity (b, green). 27

Figure 11: Entrainment versus several environmental and cloud variables in congestus clouds. The error bars represent the standard deviation of entrainment in appropriately sized bins. 33

Figure 12: ER vs updraft horizontal size (a) and median strength (b) in the 37 congestus cases with a visually identifiable, vertically coherent updraft. 33

Figure 13: Same as Figure 11, but for shallow clouds. 34

Figure 14: Entrainment vs cloud size (a), maximum buoyancy in the lowest 5 km (b), and cloud thickness (c) during the wet (green), dry (orange), and transition (blue) seasons. 37

Figure 15: Regression tree indicating the variable splits for congestus entrainment rates. The top number is the average entrainment in the group and the bottom number is the percent of total observations that are in that group. 40

Figure 16: Same as Figure 15 but for shallow entrainment rates. 41

Figure 17: The importance of each cloud and environmental variable to entrainment as found by the random forest model. Congestus results are shown in blue and shallow results are in green. 42

Figure 18: The random forest results of the relative importance of each explanatory entrainment variable in each season for congestus clouds. 43

Figure 19: Mixed layer parcel entrainment rates versus the surface-based parcel entrainment rates for a 1000 m mixed layer (a), 500 m mixed layer (b), and 100 m mixed layer (c). 45

List of Tables

Table 1: The number of congestus and shallow cumulus cases which use the best estimate of CTH, best estimate of temperature and those that use the best estimate of temperature and moisture..... 19

Table 2: Linear correlation coefficient of entrainment rate and environmental and cloud variables for both shallow and congestus. The results of the "good" cases as well as the "better" cases (parenthesis) are presented and compared to JD06..... 35

Table 3: Mean values of several variables in each the dry, wet, and transition season. These are the variables with the largest seasonal differences. 38

Table 4: R^2 values of entrainment with the environmental variables for the "better" congestus using the MWRP correction compared to cases using sounding values within 3 hours and 1 hour. 46

Table 5: Same as Table 4 but for shallow entrainment correlations..... 47

Table 6: Entrainment correlations with environmental variables for different congestus and shallow CTH definitions. “Good” shallow clouds and “better” congestus clouds are used..... 48

1 Introduction

Convective clouds are formed from rising parcels, to first order driven by buoyancy and modulated by environmental stability and mixing with environmental air. These clouds play an important role in the global energy budget by transporting heat, moisture, and momentum in the vertical and through their influence on both the shortwave and longwave radiation budget. The impact of clouds on the radiative budget depends on the cloud macrophysical (fractional coverage, thickness, and height/temperature) and microphysical (water content, particle size distribution and phase) properties. Three modes of convective clouds exist in the tropics: shallow cumulus, cumulus congestus, and deep cumulonimbus (Johnson et al. 1999).

Shallow cumulus are the most prevalent cloud type in the tropics and have cloud tops within the boundary layer (Johnson et al. 1999, McFarlane et al. 2013). They scatter the majority of incident shortwave solar radiation and thus have a net cooling effect on the surface (Bretherton et al. 2004). Surface fluxes of heat and moisture drive the destabilization the provides buoyancy for the clouds. Evaporation at cloud top moistens and cools the stable inversion layer, which balances the warming and drying from large scale subsidence. Turbulent fluxes associated with shallow cumulus therefore determine the equilibrium boundary-layer depth and thermodynamic properties (Riehl et al. 1951, Stevens 2007, Rauber et al. 2007).

Cumulus congestus clouds, defined as having cloud top heights (CTH) near the 0°C level (~5 km in the tropics), have moderate shortwave albedos (Johnson et al. 1999). Congestus are also prevalent in the subtropics and tropics, representing ~57% of precipitating convective clouds, by number, in the Coupled Ocean-Atmosphere Response Experiment (COARE) and Global Atmospheric Research Program (GARP) Atlantic Tropical Experiment (GATE) campaigns (Johnson et al. 1999). They account for 28% of the total tropical rainfall during

COARE (Johnson et al. 1999), 30% of the precipitation from GATE (Cheng and Houze 1979), and 27.3% of the rainfall over the Atmospheric Radiation Measurement (ARM) Tropical Western Pacific (TWP) Manus site (Stephens and Wood 2007). Cloud-resolving model simulations have demonstrated a wide range of congestus precipitation contribution, from 15.3-17.9% in the radiative-convective equilibrium simulations of van den Heever et al. (2011), to 34% over a 10-day onset period of the western Pacific intraseasonal oscillation (Mechem and Oberthaler 2013). From CloudSat observations, Wall et al. (2013) showed that 4% of all continental clouds are congestus and 8.5% of Amazon clouds are congestus. Further, congestus clouds are present 6% of the time in the Amazon, and they, along with deep convection, dominate the shortwave cloud radiative effect (Giangrande et al. 2017).

Both shallow cumulus and congestus cloud types play an important role in tropical climate dynamics by distributing heat and moisture vertically (Riehl et al. 1951). They also can act as a precursor for deeper convection (Neggers et al. 2007). Warm, moist air is advected by the trade winds to the intertropical convergence zone (ITCZ), which allows for increased moisture convergence and the development of deep convection (Riehl et al. 1951, Neggers et al. 2007). Despite their importance, some aspects of shallow cumulus and cumulus congestus are not fully understood and their contribution to tropical dynamics is not correctly represented in global climate models (GCMs) (Williams and Tselioudis 2007, Nam et al. 2012). GCMs underestimate the sensitivity of convection to the tropospheric humidity (Derbyshire et al. 2004), including over the Amazon region (Lintner et al. 2017). As a result, shallow cumulus and congestus cloud fractions tend to be underestimated (Williams and Tselioudis 2007, Nam et al. 2012). GCMs also do not represent diurnal cycle correctly, specifically initializing and deepening convection too quickly (Stirling and Stratton 2012).

One reason for these shortcomings may be how entrainment is represented in GCM parameterizations of convection (Del Genio 2012). Entrainment is the rate at which environmental air is mixed into a cloudy updraft and is a first-order mechanism that governs the depth to which shallow cumulus and congestus penetrate (Bretherton et al. 2004). Entrainment affects the vertical transport of heat, humidity, and momentum (Brast et al. 2016). Paluch (1979) used mixing diagrams of conservative thermodynamic variables to identify the source and mechanisms of the entrained air. Although early studies forwarded competing physical mechanisms to explain entrainment, Paluch supported Squires' (1958) conclusion that environmental air is entrained vertically at cloud top and then mixed into the cloud through penetrative downdrafts, which are created by evaporative cooling from the entrained environmental air. However, recent studies using large eddy simulations (LES) (Heus et al. 2008) and observations (Lin and Arakawa 1997) cast doubt on this cloud top entrainment theory and supported the idea of lateral entrainment. Here, environmental air is continuously entrained at lateral cloud edges into a cloudy parcel as it rises, reducing its buoyancy. Dilution is not the only consequence of entrainment. Cooper et al. (2013) found entrainment broadens the drop size distribution and enhances precipitation production.

The entrainment rate can be resolved and calculated in LES models using the bulk method (Siebesma and Cuijpers 1995, Siebesma et al. 2003) or the direct method (Romps 2010, Dawe and Austin 2012). The bulk approach uses tracers of conserved variables (such as total water) to determine the amount of mixing necessary to explain the evolution of a conserved tracer vertically transported in the cloud. The direct approach uses the velocity difference between the air and cloud surface and the movement of cloud edges to calculate entrainment directly. Romps (2010) found that the bulk method underestimates the entrainment rate

compared to the direct method. The difference between the two entrainment rates could be explained by the bulk method calculating an "effective" entrainment rate.

Because entrainment is not resolved in GCMs, assumptions must be made about its behavior. Most current parameterizations of convection are based on an entraining-plume framework, with an entrainment rate formulated as a function of various environmental or cloud properties. Some of these dependencies include inverse relationships between entrainment rates and updraft velocity (Neggers et al. 2002), cloud size (Bechtold et al. 2001), cloud thickness (Siebesma et al. 2003, Bretherton et al. 2004), relative humidity (RH, Bechtold et al. 2008, de Rooy et al. 2013), and buoyancy (Lin 1999), all supported by findings from LES. These results suggest that vertical velocity, for example, has impacts on entrainment through the amount of time available for the parcel to interact with environmental air. A slower moving parcel has more time to entrain (Neggers et al. 2002), resulting in a larger entrainment rate. Entrainment is also related to cloud depth, since, all else being equal, shallower clouds imply stronger entrainment (Bretherton et al. 2004). Moreover, a wider cloud should be able to shield its updraft core from entraining environmental air, so the buoyant core is not subjected to as much dilution by environmental air and therefore retains a stronger vertical velocity, relative to a narrower cloud (Kain and Fritsch 1990**,** Bechtold et al. 2001). The negative relationship with RH has no physical basis but yields improvements in reproducing atmospheric variability in the middle latitudes and Tropics (Bechtold et al. 2008). Finally, an inverse relationship with buoyancy can be explained by parcels with larger buoyancy will have a larger vertical velocity, and therefore less time to entrain, resulting in a smaller entrainment rate. Although these mechanistic explanations of the entrainment relationships attempt to be physically consistent, they are rather speculative and remain underexplored.

Techniques exist to estimate entrainment rate from observations. Though entrainment has been extensively studied in LES, observational estimates of entrainment are not as numerous (e.g., Jensen and Del Genio 2006, Wagner et al. 2013, Masunaga and Luo 2016, Takahashi et al. 2017, Drueke et al. 2019). Observations are more difficult to obtain due to a lack of instruments to fully sample environmental thermodynamics, cloud dynamics, and microphysics with high spatial and temporal resolution. Also, the possibility that the clouds being sampled are transient, meaning that some congestus observed could be at an intermediate point of their lifecycle and later go on to become deep cumulonimbus (Luo et al. 2009, Mechem and Oberthaler 2013). This study focuses on estimating entrainment rates and their observational uncertainties in shallow cumulus and cumulus congestus clouds during the Green Ocean Amazon 2014-2015 field campaign, using a best-estimate combination of surface-based remote-sensing instruments. These entrainment rates will be used to evaluate common entrainment closures used in GCM convective parameterizations and identify any relationships with environmental variables.

The instruments used in the study are described in section 2. In section 3, the methods for measuring observational entrainment rates and its uncertainty and assessing how it interacts with the environment are discussed. The results of the study are presented in section 4.

2 Data

Data for this project are from the Green Ocean Amazon (GoAmazon2014/5) field campaign, which took place in Manacapuru, Manaus, Brazil from January 2014 through December 2015 (Martin et al. 2016, Martin et al. 2017, Giangrande et al. 2017). One component of this field campaign was the deployment of the Department of Energy's Atmospheric Radiation Measurement (ARM) Mobile Facility (AMF, Miller et al. 2016), which includes the W-band ARM cloud radar (WACR), radar wind profiler (RWP), radiosondes, microwave radiometer profiler (MWRP), and microwave radiometer (MWR). Figure 1 shows the location of the AMF (site "T3"), which is 70 km downwind (west) of the center of Manaus (Martin et al. 2016).

The vertically pointing WACR operates at 95 GHz and has vertical gate spacing of 42.86 m and an effective temporal spacing of 2.048 s (Luke and Kollias 2013). The WACR is highly sensitive to small cloud droplets, but also severely attenuates in the presence of precipitation. The Active Remote Sensing of CLouds (ARSCL) product (Clothiaux et al. 2000, Kollias et al. 2005) combines WACR reflectivities, ceilometer, and micropulse lidar data to provide estimates of cloud properties, including cloud-base height (CBH), cloud-top height (CTH), and cloud thickness. The CBH estimate is generally from the laser-based ceilometer.

The 1290-MHz ultra-high frequency (UHF) radar wind profiler (RWP) measures backscattered radiation to determine echo boundaries and wind profiles. We use the RWP dataset processed by the methods described in Giangrande et al. (2013, 2016). The RWP has a beam width of 6°, vertical resolution of 200 m, and temporal resolution of 5 s. Since the RWP operates at a lower frequency than the WACR, it is less sensitive to small cloud droplets but also attenuates less, yielding more accurate echo boundary estimations in the presence of

precipitation. In the absence of large scatterers, the RWP may detect Bragg scattering resulting from sharp density gradients, such as those associated with inversions. Clear-air echoes are often observed in the data, illustrating the boundary layer structure. The echo classification product uses reflectivity, vertical velocity, and spectrum widths to distinguish between Bragg and non-meteorological scattering, convective cores, stratiform regions, and several other echo categories (Giangrande et al. 2013, Steiner et al. 1995).

For the duration of the campaign, radiosondes were launched four to five times daily at the ARM site, to quantify the vertical structure of the atmosphere (temperature, humidity, and winds as a function of pressure). The soundings are used to calculate the environmental lapse rate (ELR), vertical shear of the horizontal wind, convective available potential energy (CAPE), convective inhibition (CIN), lifting condensation level (LCL), and level of neutral buoyancy (LNB).

We employed two passive microwave instruments. The Microwave Radiometer Profile (MWRP) sampled the vertical characteristics of the atmosphere at about one-minute intervals, from the surface up to 10 km, using microwave radiances from 12 frequencies in the range 22-30 GHz and 51-59 GHz. It has higher temporal resolution than the soundings, but a lower vertical resolution of 100 m in the lowest 1 km and 250 m from 1 to 10 km (Liljegren et al. 2001). The instrument has a positive temperature bias and a negative moisture bias at the surface, and a positive moisture bias in the upper levels (M. Jensen, personal communication). MWRP thermodynamic profile retrievals are only accurate in the absence of precipitation. The instrument only became available for this field campaign beginning in November 2014.

The Microwave Radiometer (MWR), which observes microwave brightness temperatures at 23.8 and 31.4 GHz. Retrievals from these MWR observations (specifically the MWR retrieval

(MWRRET) product) provide vertically integrated estimates of precipitable water vapor (PWV) and liquid water path (LWP) (and uncertainties) at one-minute intervals (Turner et al. 2007).

The final dataset used in this study is the Variational Analysis (VARANAL) which contains the large-scale forcing at the site, derived from the European Center for Medium-Range Weather Forecasting (ECMWF) analysis constrained with GoAmazon2014/15 observations, local radar and satellite measurements (Tang et al. 2016). It uses the variational analysis method of Zhang and Lin (1997). The product has a vertical grid of 25 hPa and a horizontal extent of a ~110 km radius surrounding the field site. Data is produced at 3-hour intervals, resulting in 8 outputs per day. We use the large-scale pressure vertical velocity and moisture convergence from this product.

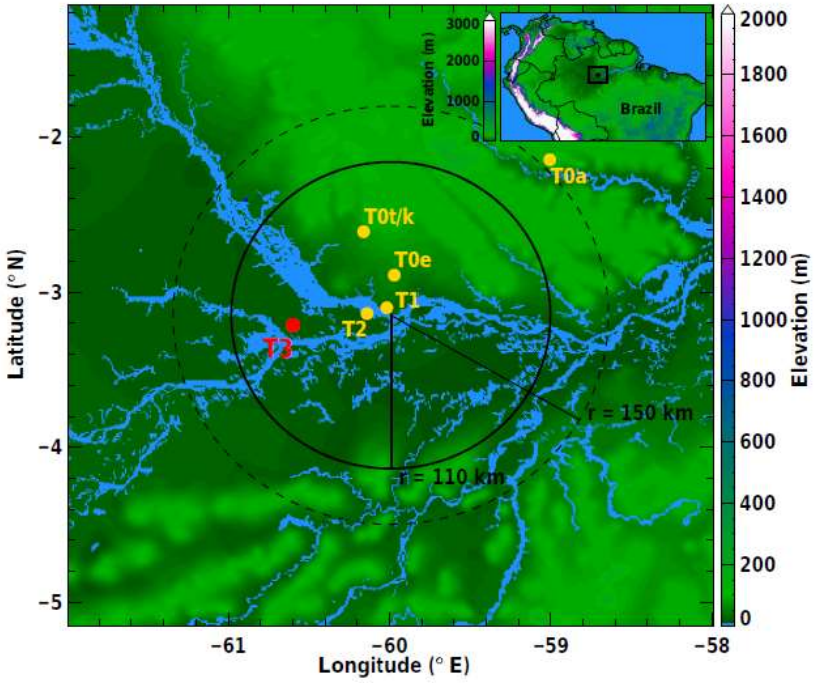

Figure 1: The location of the GoAmazon2014/5 field campaign. The AMF is located at the red dot, site T3, 70 km west of the center of Manaus (Figure 1 from Giangrande et al. 2017).

3 Methods

3.1 *Observational estimates of entrainment rate*

The entrainment rate (ER) is estimated with an idealized "entraining plume" model, which uses newly developed best estimates of maximum CTH and the thermodynamic environment to infer entrainment rates for each cumulus and congestus cloud sampled in the field campaign. The parcel is assumed to undergo linear mixing of environmental air as it ascends according to

$$\theta_{ep}\ (z + \Delta z) = \left[\frac{\theta_{ep}(z)+\varepsilon\Delta z\theta_e}{1+\varepsilon\Delta z}\right], \quad (1)$$

where θ_{ep} is the equivalent potential temperature of the parcel, θ_e is the equivalent potential temperature of the environment, and ε is the entrainment rate (Jensen and Del Genio 2006, hereafter JD06). This method assumes θ_e is conserved in adiabatic motions and environmental air is mixed into the parcel linearly at a constant rate of ε. Entrainment rate is found iteratively, starting with an initial value of ε = 0.01 km^{-1}, and then increasing ε in increments of 0.001 km^{-1} until the [entraining] level of neutral buoyancy (ELNB) coincides with the CTH. The ELNB is the last height at which the θ_{ep} is greater than θ_e. The θ_e profile is smoothed in the vertical using a moving average with a window width of 150 vertical grid points (~1.5 km) to minimize fine-scale variations. The initial entrainment rate is very small (practically zero, a nearly undilute parcel), so the ELNB should be higher than the observed CTH. As the entrainment is increased, the ELNB will decrease (Figure 2) (JD06).

Caveats of this method include the theoretical assumptions underlying the approach, specifically that convection can be represented by an idealized plume undergoing continuous, lateral entrainment with height. Although historically the plume approach has been used in models, convection may be better represented by a series of transient thermals. If this were the

case, each thermal would grow in a subsequently moister environment, entrain higher θ_e air, and grow taller than the previous thermal. Entrainment estimates assuming the plume model would be lower than those found using the thermal approach, since the plume entrains lower θ_e air, requiring less mixing to sufficiently dilute the parcel. The method also requires an accurate measurement of the CTH, a representative thermodynamic environment, and an assumption about initial parcel thermodynamic properties. This entraining-plume method can only provide entrainment rate estimates for clouds passing directly over the radar and therefore constitutes a sample of the total cloud population. This method also assumes the maximum cloud height for any given cloud sampled by the radar is associated with the strongest updraft and therefore smallest value of entrainment. In reality, we are not always sampling the strongest updraft or center of every cloud that passes over the radar. Assuming we are sampling along a random chord of a circular cloud, we could be underestimating the cloud size by 22% (Jorgensen et al. 1985). If the cloud shape is ellipsoidal rather than circular, the bias in cloud size could be as high as 32% (Borque et al. 2014). How this chording bias relates to any potential bias in CTH is not obvious but is beyond the abilities of our observations to address.

This method fails when the parcel θ_e (θ_{ep}) is very similar to the environmental θ_e. The parcel entrains this high θ_e air, so no matter how much environmental air is entrained, the ELNB will not decrease enough to equal the CTH, and an entrainment rate cannot be estimated (Figure 3). The reason for this problem is not obvious but could have multiple causes associated with the CTH, environmental profile, or assumed initial parcel properties somehow being unrepresentative of the cloud being observed. This problem occurs in a small number (10%) of the cases, so the sample size of clouds used in this study is smaller than the total number of clouds observed in the campaign.

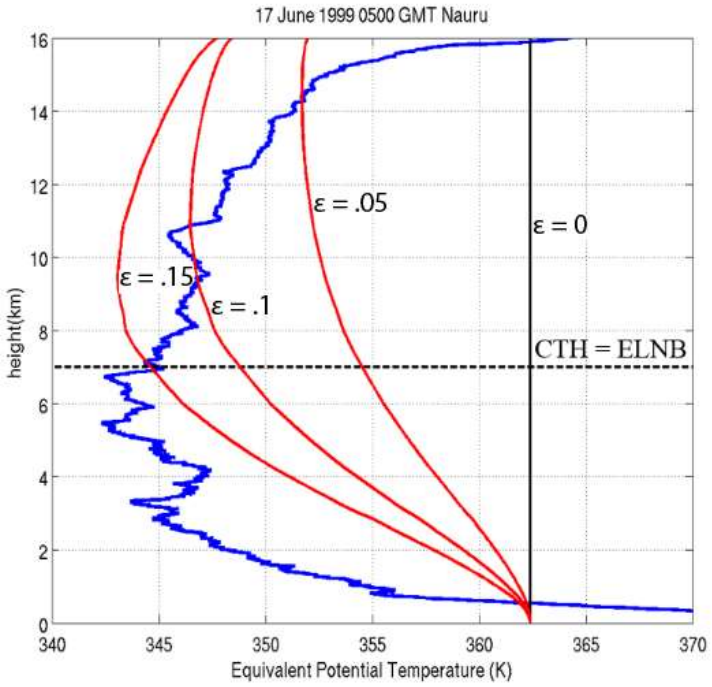

Figure 2: The "entraining plume" model used to find the entrainment rate. The blue line represents the environmental θ_e. The black line is the undiluted parcel θ_e, and the red lines are the parcel θ_e experiencing different amounts of entrainment. Here, the entrainment rate is 0.15 km^{-1} since that is the rate at which the CTH equals the ELNB.

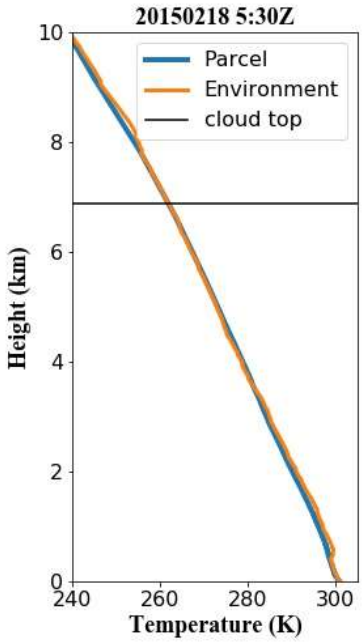

Figure 3: The virtual temperature profiles of the environment and parcel. The parcel virtual temperature will never be less than the environment below CTH and thus an entrainment rate for this case cannot be calculated.

3.2 *Best estimate of CTH*

Contiguous (neighboring) profiles where ARSCL reflectivity and mean Doppler velocity (MDV) are both defined are identified as cloud. To be included in the analysis, the cloud must have a maximum height between 1 and 9 km and be sampled for more than 60 s.

As mentioned previously, the WACR strongly attenuates in the presence of precipitation (Haynes et al. 2009), resulting in an underestimate of CTH which will lead to an overestimate of the entrainment rate. The lower-frequency RWP attenuates less, yielding a more accurate estimate of CTH when clouds are precipitating or otherwise have large droplets. For this reason, we use the RWP in combination with the WACR to form a best estimate of CTH for all cloud cases. The RWP echo classification product (Feng and Giangrande 2018) is used to distinguish between Bragg and Rayleigh scattering. The RWP CTH is taken to be the maximum height of the echo classified as either "convection," "weak convection," or just "cloud." The multi-instrument best estimate of the CTH is the maximum value of the ARSCL and RWP CTH values (Figure 4).

Figure 5 shows the importance of using the RWP to improve our estimates of CTHs. Most RWP CTHs are much larger than the ARSCL CTHs because of beam attenuation of the WACR. The CTH estimates from the RWP are, on average, 1.3 km greater than the ARSCL CTHs. For some clouds, RWP estimates of CTH lie above 9 km (deep convection), whereas the ARSCL (WACR) product would classify the same cloud as congestus, since the radar beam is extinguished well below reaching cloud top. The cases where the ARSCL CTH is larger than the RWP occur because the RWP is not sensitive enough to observe the total cloud. The majority of the shallow clouds are missing from this plot because they do not have large enough hydrometeors to be detected by the RWP, and the cloud is classified in the 'Bragg and Insects'

category. Therefore, an RWP CTH is not measured. In this case, the ARSCL CTH is assumed to represent the best estimate of CTH.

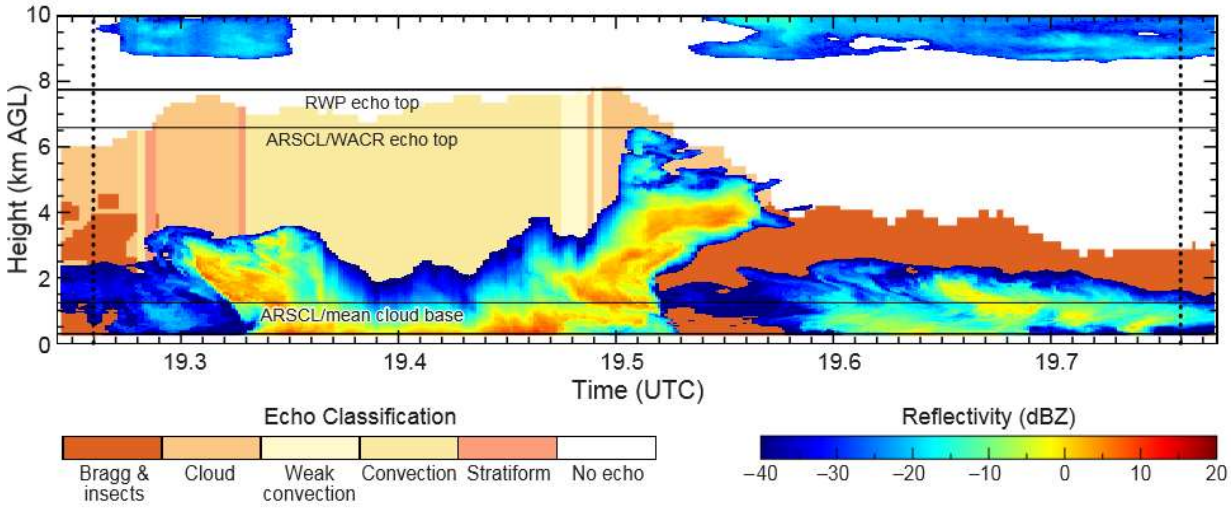

Figure 4: The WACR reflectivity and RWP echo classification for a congestus cloud on April 4th, 2014. The WACR is clearly attenuating due to the precipitation and does not sample the entire cloud. Therefore, we use the RWP-sampled CTH.

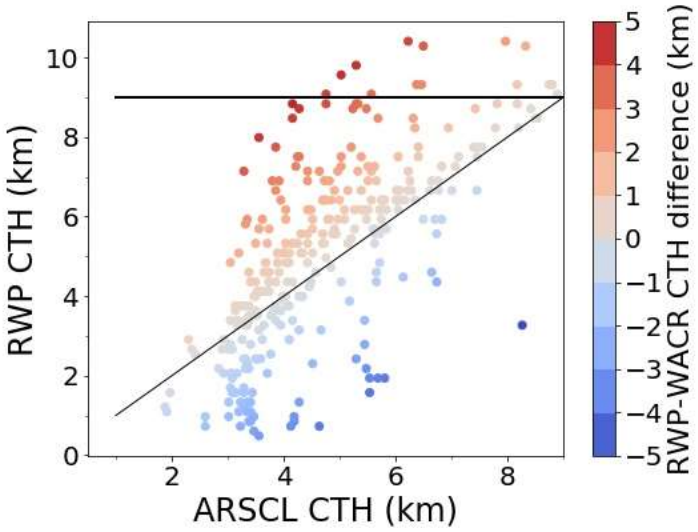

Figure 5: The RWP CTH vs ARSCL CTH color-coded by the CTH difference. The red points indicate that the RWP is larger and the blue points indicate that the ARSCL CTH is larger. The horizontal black line represents the upper-limit of congestus clouds (9km) and the diagonal black line is the 1:1 line.

Each cloud is separated into shallow cumulus and cumulus congestus based on the CTH best estimate. Shallow cumulus are defined as those having a CTH greater than 1 km and less than 3 km and a CBH less than 1 km. We further require the shallow cumulus to be active to avoid having convection forced by mechanisms other than buoyancy. Active clouds are defined as having a layer of positive buoyancy (Stull 1985) and thickness greater than 300 m (Zhang and Klein 2013). In any case, forced clouds are automatically filtered out since an entrainment calculation for them would fail because they lack positive buoyancy.

Congestus are defined as having CTH between 3 and 9 km and CBH less than 1 km. The depths for the classifications vary across different studies and are somewhat arbitrary. The lower bound (3km) of congestus is consistent with the approximate upper bound of shallow cumulus (Mechem and Oberthaler 2013). The upper bound (9 km) of congestus is chosen to include congestus clouds that penetrate above the 0°C level and to be consistent with previous work on the topic (Johnson et al. 1999, Jensen and Del Genio 2006). A total of 207 active shallow cumulus and 686 congestus were identified during the GoAmazon2014/5 deployment. However, these numbers are reduced when only considering the clouds that occur during the time that the MWRP was operating. Further, the limited number of clouds that have a successful entrainment estimation are 67 shallow and 415 congestus. Figure 6 shows a histogram of all shallow and congestus CTHs used in this study.

We recognize that the peak occurrences in CTH (Figure 6) do not exhibit the ideal bimodal distributions of shallow cumulus and congestus clouds. However, the CTH definition for shallow cumulus of 1-3 km is still a good choice for the Amazon region. Figure 9g of Giangrande et al. (2020) shows a peak in cloud fraction at a height of 2 km, falling to a minimum in frequency around 3 km, indicating that the majority of the shallow clouds in the campaign fall

into this definition. Though shallow cumulus are the most prevalent cloud type observed during the campaign (Giangrande et al. 2017), our methods filter out a significant portion of the dataset, for various reasons, including a lack of positive low-level buoyancy and clouds with small thicknesses. We only use the shallow clouds that result in a sensible entrainment rate calculation.

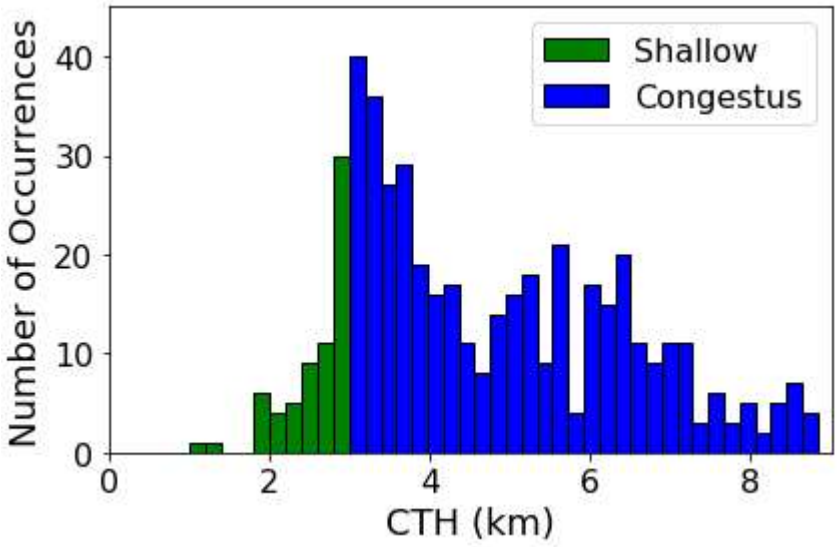

Figure 6: A histogram of cloud top heights of all the clouds used in this study. Shallow have CTH < 3 km and congestus have CTH between 3 and 9 km.

3.3 *Best estimate thermodynamic profile*

Because radiosondes are only launched every six hours, the sounding used in the entrainment rate calculation may be up to six hours prior to the start of the cloud (soundings used from periods after the cloud may be influenced by convective mixing events), in which case the sounding may not be representative of the thermodynamic environment in which the cloud grew. Temperature and moisture profiles from the MWRP are employed to produce more representative thermodynamic profiles than the soundings alone. The MWRP has improved temporal resolution relative to the 6-hourly soundings, but the absolute values of temperature and

moisture are biased (M. Jensen, personal communication), so the MWRP profiles cannot be used directly. In addition, the vertical resolution of the MWRP is coarser than the soundings, and the retrieved profiles smooth out important details needed for the entrainment calculation. To overcome these shortcomings, we use the relative differences of the MWRP temperature and moisture profiles between the time of the cloud and time of the most recent sounding as a correction to the radiosonde temperature and moisture profiles. The best-estimate procedure is shown in Figure 7. The largest changes between the sounding and the cloud occur in the boundary layer (lowest 3 km), with only small corrections above 3 km. For the majority of cases, the largest temperature correction is at the surface, which is consistent with strong solar heating and a boundary layer being heated from the surface. For some cases, the MWRP temperature correction (difference) is not at the surface but rather just above. This would suggest a stabilization of the boundary layer under strong surface heating, which we viewed as unphysical. In these cases, we instead extend that maximum correction down to the surface.

We further constrain the moisture profile using the MWR precipitable water vapor (PWV) retrieval (Turner et al. 1998). The moisture profile is adjusted until its PWV equals the MWR PWV (Figure 7b). Above 10 km altitude when no MWRP profiles are available, the most recent sounding is assumed to be representative. In 40% of the data (191 cases), this process results in layers of supersaturation of about 104% RH on average. Therefore, we decrease the mixing ratio iteratively in these layers until the RH equals 100%. The MWRP and MWR retrievals fail when the instrument window is wet from precipitation (as indicated by error flags), in which case they cannot retrieve good quality data due to moisture on the instrument. Another error flag occurs if the retrievals of mixing ratio and temperature result in supersaturation. If either of these situations occur, the data are searched up to one hour prior to the start of the cloud

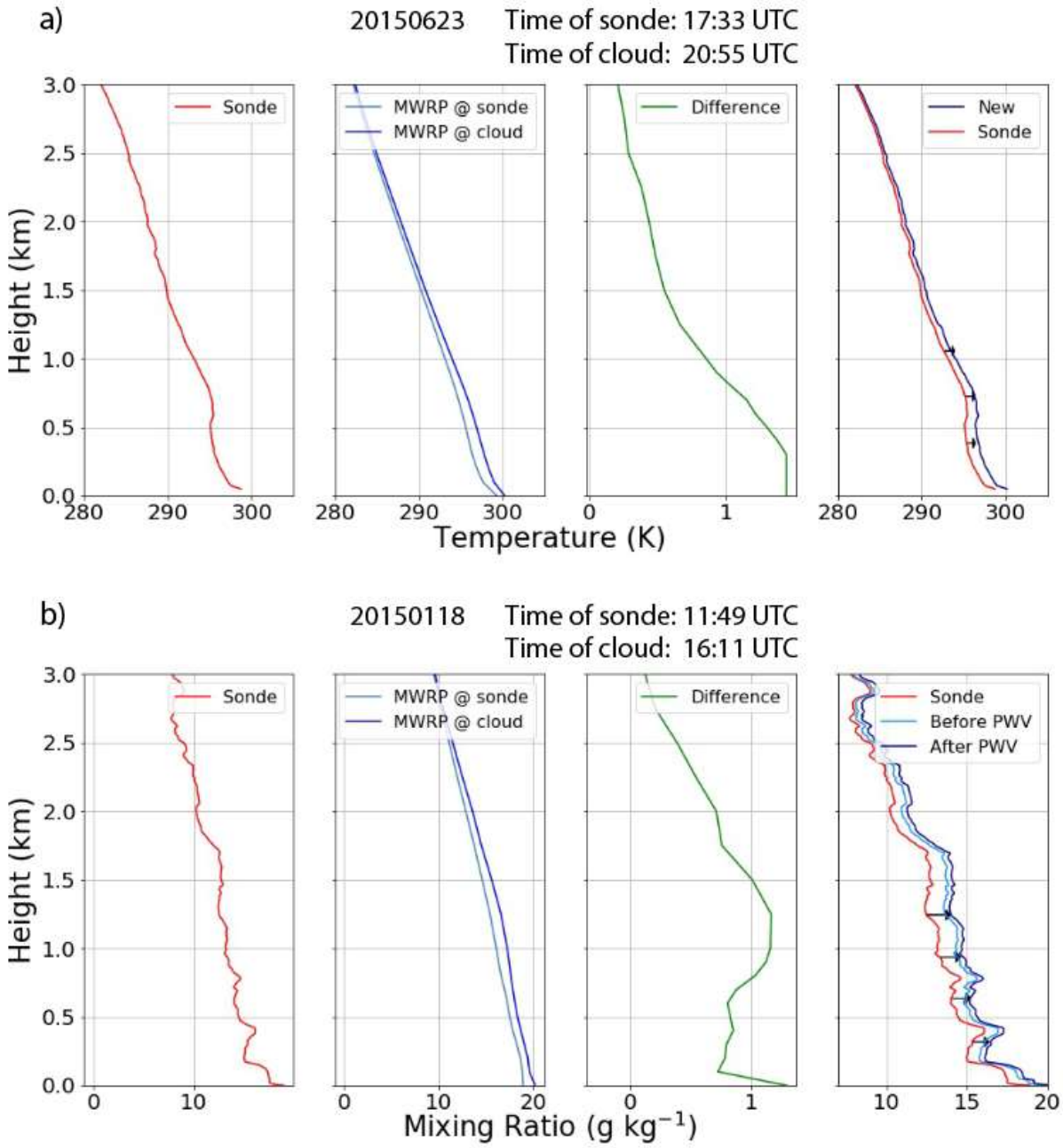

Figure 7: Vertical profiles of the radiosonde, MWRP at the time of the sounding and cloud and their difference, and corrected profile temperature (a) and mixing ratio (b).

for good data. If no MWRP or MWR retrievals are available within an hour of the start of the cloud, the radiosonde observations alone are used for the entrainment calculation. If no good MWRP retrievals are available, we also do not use the MWR since it does not make sense to correct the moisture, but not the temperature. Table 1 shows the amount of cases which have

good quality MWRP and MWR retrievals available and therefore use the best estimates of temperature and moisture profile.

Most of the thermodynamic profile corrections applied to the soundings resulted in an increase of temperature and moisture in the boundary layer. Over half of the clouds occur between the 1100 UTC (0700 LT) and 1700 UTC (1300 LT) soundings during the part of the day when the temperature is increasing the most due to radiational heating. However, about 20% of the clouds occur between 0500 UTC (0100 LT) and 1100 UTC (0700 LT) when the temperature is decreasing, and therefore have a best-estimate of temperature which is lower than the nearest prior sounding temperature.

CAPE is a measure of the stored potential energy in the atmosphere and increases as boundary layer temperature and moisture increases. Figure 8a shows the CAPE calculated from the best estimate thermodynamic profiles versus the CAPE calculated from the radiosonde profiles themselves. Since the majority of the corrections add temperature and moisture, the CAPE in the lowest 5 km is larger in the majority of the MWRP corrected parcels, though there are some cases where the CAPE from the radiosonde alone is larger, corresponding to the 20% of cases where the temperature and moisture decreased. Figure 8b shows the CIN decreases when the correction is applied, making the environment more conducive for convection. However, the correction does not alter the mid-level environmental lapse rates (ELR) much (Figure 8c). The largest CAPE corrections are due to surface and boundary layer changes as the day progresses.

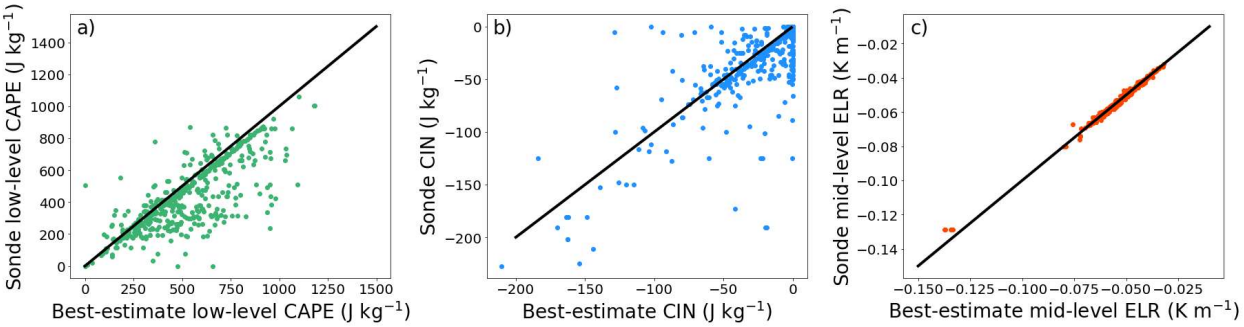

Figure 8: A comparison of the MWRP thermodynamic best estimate to the sounding using stability variables: low-level CAPE (a), CIN (b), and mid-level ELR (c).

Table 1: The number of congestus and shallow cumulus cases which use the best estimate of CTH, best estimate of temperature and those that use the best estimate of temperature and moisture.

	Total (Best estimate CTH)	Good MWRP	Good MWRP & MWR
# of congestus cases	415	275	183
# of shallow cases	67	33	25

3.4 *Best estimate entrainment rates*

The best estimate cloud top heights are either larger than or equal to the ARSCL CTHs, with most of them being larger. In our method, higher CTHs require less dilution due to environmental mixing and therefore, smaller ERs. The increases and improvements in CTH result in decreases in the ER compared to those that only use the ARSCL CTHs (Figure 9a). The ERs decrease on average 0.078 km^{-1} (13.6% change).

Most of the best-estimate profiles are warmer and moister compared to the sounding they are based on, which results in a larger entrainment rate compared to that calculated based on the sounding alone. The larger entrainment rate is required to sufficiently dilute the buoyancy of a parcel having warmer and moister initial properties such that the ELNB lies at the radar-

estimated CTH. Likewise, when decreasing the temperature and moisture of the initial parcel it is expected that the entrainment rate will also decrease. Therefore, the entrainment rates may either increase or decrease when the corrections are applied to the thermodynamic profiles (Figure 9b). Figure 9b also shows that as the time between the nearest prior sounding and the cloud increases, the correction also increases, as expected. Relative to the estimate of entrainment rates using solely the most recent soundings, the thermodynamic best estimate yields a mean entrainment rate change of 0.0995 km^{-1} (25% change). Our best approach using more representative estimates of cloud top and thermodynamic profiles should yield improvements in calculated entrainment rates.

For about a third of the cases (157), the MWRP was not available so the profiles from the most recent sounding were used. The reason for this was typically a failure of the MWRP retrieval because of a "wet window" or other bad data quality flag.

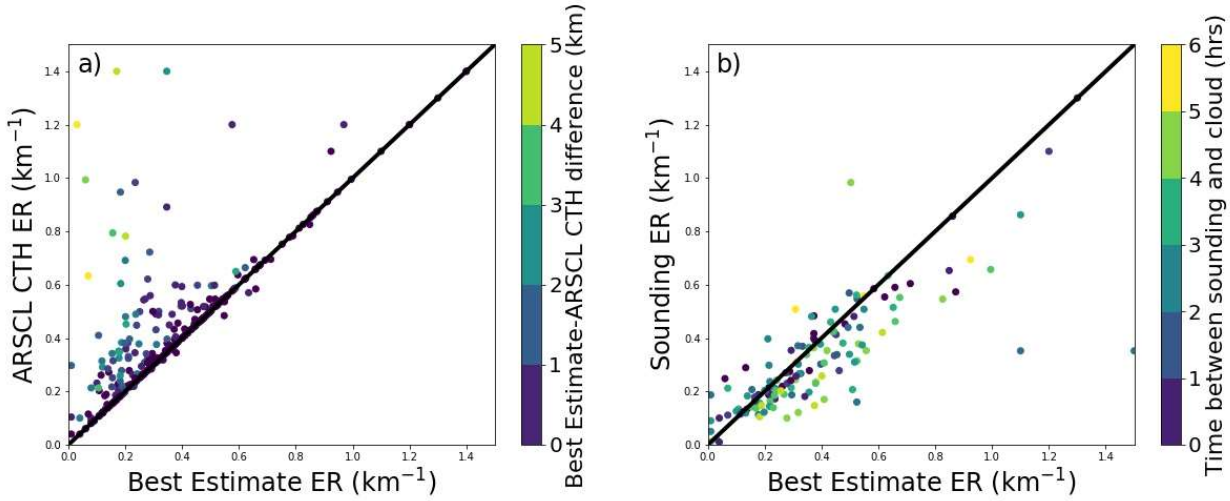

Figure 9: The ER calculated using ARSCL CTHs and best estimate thermodynamic profile versus the ER calculated from the best estimate CTH and thermodynamic profile, color-coded by the difference between the best estimate CTH and ARSCL CTH (a). The ER calculated using the sounding thermodynamic profiles and best estimate CTH versus the ER calculated from the best estimate CTH and thermodynamic profile, color-coded by the time difference between the cloud and sounding (b). The black line is the 1:1 line.

3.5 *Evaluating environmental controls on entrainment rates*

Environmental controls on entrainment rate will be explored to evaluate common entrainment closures, understand the physical mechanisms of entrainment, and identify other variables not commonly used in closures but potentially impact entrainment rates. A linear regression is performed of the entrainment rate and each environmental variable, including surface-based CAPE, CAPE in the lowest 5km, RH in various layers, horizontal wind shear, environmental lapse rate (ELR **,** over 1-3km and 3-6km layers), maximum buoyancy in the lowest 5 km, vertical velocity at 700 mb, and the vertical integral of moisture convergence. We focus on the ER relationship with CAPE and buoyancy in the lowest 5 km to be more representative of shallow and congestus cloud growth environments.

Correlations between entrainment and cloud properties, including cloud depth and cloud size are also found. The cloud depth is the best estimate CTH minus the ARSCL CBH. The cloud size is calculated using the length of time of the cloud and the average wind speed (from the radiosonde) in the cloud layer. Recognizing that the entrainment is likely better correlated with the updraft width, we attempt to identify updrafts by first subtracting out the hydrometeor fall speeds from the RWP mean Doppler velocity (MDV). This can be done using a simple parameterization of the hydrometeor fall speed as a function of RWP reflectivities (Z) (Giangrande et al. 2016). The fall speeds are also adjusted by the height (H [m]) to account for the change of air density with height, since drops will fall faster in less dense air:

$$V_{fall} = 2.65 * Z^{0.1} * e^{H/20000} \quad (2)$$

The vertical motion of the air in the cloud is then:

$$V_{air} = MDV - V_{fall} \quad (3)$$

The width of the updraft is found by visually identifying the updraft core ($V_{air} > 0$) and then transforming it to a physical width by multiplying the updraft time by the average wind speed in the cloud layer, just as for the cloud itself. We are only able to visually identify vertically coherent updrafts in 37 of the clouds, presumably because the full updraft cores in the other clouds do not pass over the WACR/RWP location.

We calculate the coefficient of determination (R^2) among different variables, but because the variables are not independent, we do not expect the sum of the R^2 to be 1. The data are separated according to shallow and congestus clouds and by wet, dry, and transition seasons to explore whether entrainment varies according to cloud regime or season. The wet season is identified as December, January, February, March, and April (Giangrande et al. 2017). The dry season is June, July, August, and September, and the transition season is May, October, and November. The dry and wet seasons have pronounced differences in mid-level RH. The afternoon dry season average RH is 31%, whereas the wet season average is 68%. The wet season also has values of CAPE and CIN which are slightly more conducive to convection than in the dry season (Giangrande et al. 2017). We expect our entrainment rate estimates to vary slightly throughout the year due to the changes in RH. The results are further separated by "good" and "better" cases, where "good" includes all of the clouds where the entrainment estimation method behaves properly and an entrainment rate is able to be calculated, and "better" excludes those where the radar CTH – ELNB is greater than 400 m to ensure that the entrainment and cloud top proxy (ELNB) are representative of the actual observed cloud. We find 415 "good" congestus, 67 "good" shallow, 210 "better" congestus, and 20 "better" shallow.

Although simple linear regression provides a basic idea of how individual variables influence entrainment rate, the relationships among the different variables are likely highly

covarying, and the influence of the variables on the entrainment rate is nonlinear. For this reason, a broader array of statistical methods is needed to identify and explore possible relationships between variables. We use regression trees and random forests to evaluate the environmental controls on entrainment rate.

Regression tree methods are used to predict a dependent variable using continuous, nonlinear predictor variables (Breiman 2001). Several input (predictor) variables are used to predict the dependent variable using recursive binary splitting to group similar data. The model iterates through all variables and multiple thresholds of each variable to find an optimal bifurcation. The optimal split is one that minimizes the sum of the squares between the observations and mean of each group. Further splits, or branches are created off of existing branches, until no more splits can be made, and each node is as homogeneous as possible. We use the 'Rpart' R package based off the methods in Breiman et al. (1984) to create the trees. The depth of the tree and other model tuning parameters can be controlled with cross validation techniques to avoid overfitting the data (Kuhn and Johnson 2013) in which case the model would not be a good predictor of other data introduced. Cross validation uses a subset of the full dataset to train the model, and then the model is tested on the remaining subset of data. In this case, the training data is a random 80% sample of the data and the other 20% is the test data. 10-fold cross validation with 1000 repeats is used. The model with the smallest root mean square error (RMSE) between the trained model and test model is chosen as the final model. Repeating this process several times allows us to identify the values of the tuning parameters, particularly the maximum depth of the tree. We find that adding a 6^{th} level to the tree does not decrease the complexity parameter or error rate by much. Therefore, we choose the maximum depth of our tree to be 5. Please see Breiman et al. (1984) for more detail on the regression tree method.

Regression trees tend to be highly sensitive to thresholds that determine the branching bifurcations, whereby errors in predictor variables can produce large errors in the dependent variable. Further, a single regression tree is more likely to overfit the data. However, using an ensemble of regression trees, a random forest, helps to reduce these problems. A random forest randomizes the order the variables are split and allows only a certain subset of predictive variables to be considered at each split. Therefore, an ensemble of random, diverse trees is more likely to have offsetting biases. Please see Breiman (2001) for more details on random forests. All the environmental variables are input into a random forest to identify the variables with the largest effect on entrainment rate. The data is subset into random training and test samples, and 10-fold cross validation is used to validate the model, as in the regression tree. The best model with the smallest error between the predicted and observed data is then found. The regression trees and random forests are done separately for both shallow and congestus clouds and the results are compared to see whether entrainment interacts differently with the environment in two different cloud regimes. Differences in interaction variables are also compared between the wet, dry, and transition seasons.

3.6 *Quantifying measurement uncertainty*

Uncertainty in entrainment rates arise from different sources, broadly speaking 1. instrumental and retrieval uncertainties; 2. sampling issues; and 3. appropriateness of the bulk-plume method. Our uncertainty estimates are based on instrumental and retrieval uncertainties that are well characterized. We acknowledge the presence of sampling challenges and limits of the bulk-plume method but quantifying those uncertainty estimates is beyond our ability.

We quantify uncertainty using standard error propagation techniques (Taylor 1982). Measurement uncertainty is partially due to the limited precision of instrument sampling,

resulting in random errors, and instrument or calibration biases, resulting in systematic errors. We are interested in quantifying the uncertainty in our entrainment rate estimations due to the random instrumental uncertainty. Unless informed otherwise, we assume the instruments are properly calibrated.

Uncertainty in the measured CTHs is attributable to the minimum detectable signal of the RWP. The RWP range gate spacing (200 m, Giangrande et al. 2016) is used as the uncertainty in the CTH. This error is then propagated through to the entrainment rates by increasing and decreasing all of the CTHs by 200 m, computing the entrainment rates, and comparing those entrainment rates to the original rates. Although the WACR range gate spacing is smaller (42.86 m), to be conservative and avoid confusion we use 200 m as an uncertainty for all CTH measurements.

Assessing the uncertainty in the thermodynamic profile is less straightforward, since we use a combination of several instruments and retrievals with different uncertainty characteristics. The uncertainty in the sounding temperature profile is ±0.5 K (2σ from the mean) throughout the profile (Holdridge et al. 2011). The uncertainty in the MWRP temperature retrieval is ±1-2 K in the lowest 2 km and ±3-4 K from 2-10 km (2σ from the mean, Cadeddu and Liljegren 2018**)**. Therefore, we use ±1.5 K in the lowest 2 km and ±3.5 K above for the MWRP temperature uncertainty. Above 10 km we assume the uncertainty estimate associated with the radiosonde observations. The temperature uncertainty is the sum of squares of the MWRP and sounding uncertainty in each of the layers. The profile is then smoothed to remove sudden changes in the vertical temperature (Figure 10a).

The sounding relative humidity measurement uncertainty is ±5% (Holdridge et al. 2011). The MWRP vapor density measurement uncertainty is 20% of the total vapor density profile

(Cadeddu and Liljegren 2018), which corresponds to vapor density values of approximately ±1 gm^{-3} in the lowest 3 kilometers and ±0.1 gm^{-3} from 3 to 10 km. The MWR PWV measurement uncertainty reported in Cadeddu et al. (2013) is ±0.05 cm. The standard deviation surrounding the measurement of PWV at the time of the cloud is ±0.1 cm (1σ, Gaustad and Turner 2007). We choose to use the larger of the two values (0.1 cm), even though the value includes PWV variability as well as measurement uncertainty.

The moisture profile is broken down into 4 levels: 0-3 km, 3-6 km, 6-10 km, and 10+ km, and the uncertainty is calculated in each of the layers. All of the instrumental uncertainty measurements are converted to mixing ratio units, g kg^{-1}, using a representative temperature and pressure in the layer. The total uncertainty profile is found using the sum of squares of all three instrumental uncertainties. The values are then converted to relative humidity for the ER calculation, with the uncertainty profile shown in Figure 10b.

The majority (96%, 2σ) of temperature and moisture retrievals lie within the uncertainty profiles in Figure 10. However, we propagate the uncertainty in temperature and moisture using the 1σ values. Therefore, the entrainment rate uncertainty is reported as 1 standard deviation away from the mean. An idealized cloud, with a CTH of 6000 m and an ER or 0.298 km^{-1} is used as the control in finding the thermodynamic uncertainties. The temperature and moisture uncertainty (±1σ) profiles are added to and subtracted from the ideal case temperature and moisture profiles, in all possible combinations. These new uncertainty profiles are substituted into the entrainment calculation to find the changes in ER from the idealized case. Some of these choices seem somewhat arbitrary but are necessary given the overwhelming number of degrees of freedom especially in the height-dependent uncertainties of the retrieved thermodynamic profiles.

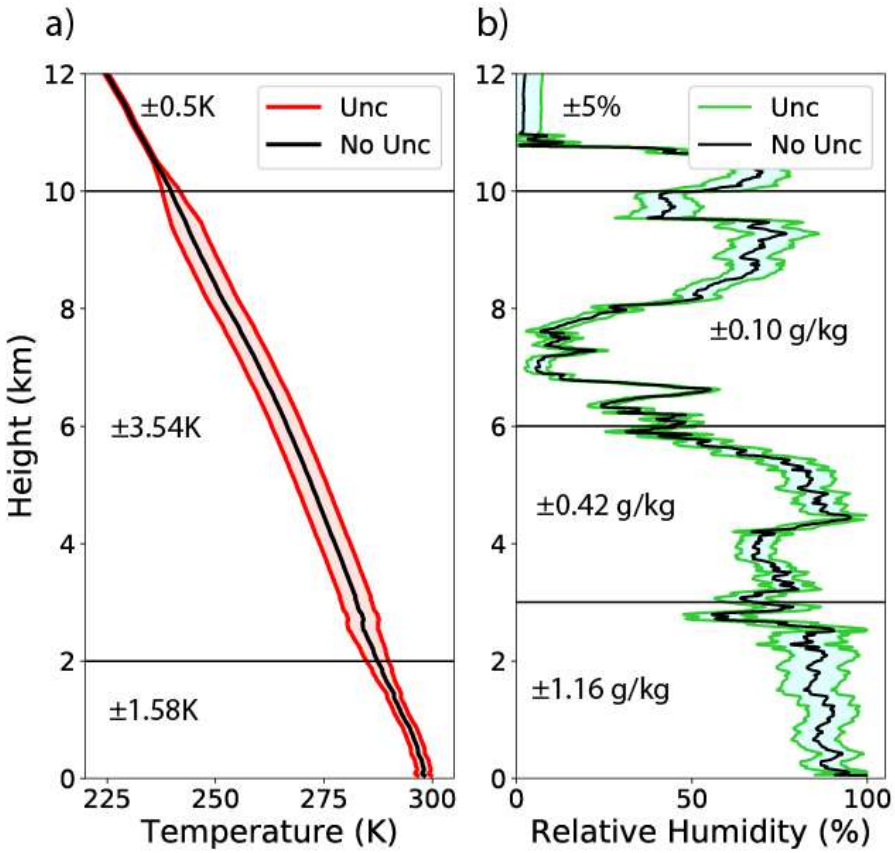

Figure 10: Idealized temperature and relative humidity profiles adapted from June 28, 2015 at 17:44Z (black) with the addition and subtraction of the instrumental uncertainty profiles and the magnitudes of the uncertainty in each level for temperature (a, red) and relative humidity (b, green).

3.7 *Sensitivity tests*

Some uncertainties in the analysis arise from the choices made in the entrainment rate calculation. These choices include how the initial parcel properties are formulated, the impact of additional MWRP/MWR retrievals on the environmental thermodynamic profiles, the specific definition of shallow and congestus clouds, and the choice of pseudoadiabatic vs reversible ascent.

Parcels that ultimately form cumulus clouds generally originate at the surface (Lin 1999) but using surface properties for the initial parcel may yield a parcel that is too buoyant. The actual parcel thermodynamics may be better represented by mixed-layer properties. The

entrainment sensitivity to different assumptions about the initial parcel, including using surface-based and parcels originating from the lowest 100 m, 500 m, and 1 km mixed-layer, will be quantified.

Since the sounding could have measured the thermodynamic profile up to 6 hours prior to the time of the cloud, the measurements may not be representative of the environment in which the cloud grew. The MWRP corrections help to quantify the environmental state at the time of the cloud observation, but it has biases and low vertical resolution. We compare the correlations between entrainment rate and different explanatory variables when using our best estimate thermodynamic and CTH to those found when using the sounding for cases where the sounding profile is within 3 hours and 1 hour from the cloud occurrence.

Johnson et al. (1999) identifies shallow clouds as having CTH less than 3 km, but this specific number is somewhat arbitrary, so we test the sensitivity of our definition of shallow cumulus and congestus clouds. We explore this sensitivity of shallow clouds by defining them as having a CTH below 4 km, to better match the bimodal distribution of CTH in Figure 6. The resulting congestus clouds then have CTH between 4 and 9 km.

Pseudoadiabatic ascent assumes all of the water that is condensed is immediately rained out, whereas moist adiabatic ascent preserves the total water in the parcel, leaving it available for evaporation if the parcel descends (whereas the pseudoadiabatic parcel will follow the dry adiabat upon descent). In reality, neither of these extremes occur and the actual parcel ascent is somewhere in between. The assumption of pseudoadiabatic ascent overestimates the entrainment rate because it does not take into account hydrometeor loading so the parcel will be more buoyant relative to moist adiabatic parcel ascent. The entrainment sensitivity to the ascent condition is quantified.

4 Results

4.1 *Entrainment rates*

Our best-estimate entrainment rates in congestus range from 0.19 to 0.94 km^{-1}, with an average of 0.57 km^{-1} and standard deviation of 0.31 km^{-1}.The shallow cumulus entrainment rates range from 0.63 to 1.7 km^{-1} and have an average entrainment rate of 1.2 km^{-1} and standard deviation of 0.46 km^{-1}. JD06 found similar entrainment rates ranging from 0.1 to 0.68 km^{-1} in 67 congestus clouds from Nauru Island in the Tropical Western Pacific. Lu et al. (2018) found entrainment rates measured from a bulk-plume model ranging from 1-3 km^{-1} in continental shallow cumulus, and Siebesma et al. (2003) found fractional entrainment rates of 2.0 km^{-1} at the bases of marine trade cumulus. Our rates are similar to those found observationally by Lu et al. (2018) but about half the magnitude of those in the LES simulations of Siebesma et al. (2003). Because of the greatly different approaches to calculating entrainment between the bulk observational method of JD06 and the bulk tracer LES approach in Siebesma et al. (2003), we should not necessarily expect perfect agreement. The two calculations essentially represent different definitions of entrainment.

4.2 *Observational evaluation of entrainment closures in atmospheric models*

4.2.1 Linear regression

The results of the linear regression analysis between the entrainment rates and environmental and cloud variables for shallow cumulus and congestus are shown in Table 2. The ER and explanatory variable correlations of the “better” category are slightly improved from the “good” category. However, the R^2 values change significantly between the two categories for the shallow clouds, probably due to the small sample size.

LES studies have found relationships between entrainment and cloud thickness (Siebesma et al. 2003, Bretherton et al. 2004), cloud lateral size (Kain and Fritsch 1990, Bechtold et al. 2001), vertical velocity of the updraft (Neggers et al. 2002), RH (de Rooy et al. 2013), and buoyancy of the updraft (Lin 1999). We evaluate these relationships to try to provide some observational constraint to the LES findings.

Entrainment rates in GoAmazon congestus clouds have the strongest relationship with the maximum buoyancy in the lowest 5 km ($R^2 = 0.16$). This agrees with the results of JD06 who found a correlation with $R^2 = 0.19$ over a smaller number of cases (67) of maritime congestus clouds. However, not all studies agree on the relationship between entrainment and buoyancy. Lin (1999) uses a cloud resolving model (CRM) and finds an inverse relationship between cumulus entrainment and buoyancy. Our results show a negative relationship between ER and buoyancy (Figure 11a), consistent with Lin (1999) and the idea that a cloud with larger buoyancy will have a larger vertical velocity, less time to entrain, and smaller ER (Neggers et al. 2002).

Entrainment is also moderately correlated with cloud thickness, which explains about 13% of the variance in ER. This relationship is negative (Figure 11b), in agreement with the model parameterizations which prescribe entrainment as inversely proportional to the depth, i.e.,~1/*H* (Siebesma et al. 2003). The interpretation for this relationship is straightforward. For parcels with similar values of initial buoyancy, those experiencing less entrainment (smaller entrainment rates) will be taller.

Early fluid tank experiments found an inverse relationship between entrainment and plume radius (Morton et al. 1956, Turner 1969) leading to parameterizations of entrainment with the same relationship (Kain and Fritsch 1990, Bechtold et al. 2001). Due to chording, we do not sample every cloud's updraft, nor the center of the updrafts we do sample. We use the total

lateral cloud size, which includes the updraft plume, to analyze this relationship. Cloud size explains about 11% of the variance in entrainment and is a negative relationship (Figure 11c), in agreement with LES. We are able to observe vertically coherent updrafts in 37 congestus clouds. In these clouds, entrainment is relatively moderately correlated with the updraft lateral size (R^2=0.12, Figure 12a), with a negative relationship in agreement with LES. However, in clouds where a coherent updraft could be identified, the median of the updraft velocity is not correlated with entrainment (Figure 12b), despite the LES findings of Neggers et al. (2002), who find an inverse relationship between entrainment and the vertical velocity of the updraft. Grant and Brown (1999) conversely, find a positive relationship between entrainment and updraft velocity in LES and suggest that larger vertical velocities drive a larger amount of turbulent kinetic energy (TKE) production, resulting in a larger entrainment rate.

The final entrainment closure to evaluate is a negative relationship with environmental RH. However, like buoyancy and updraft velocity, the relationship is not agreed upon between different LES studies and observations. Some LES studies have found a negative relationship (de Rooy et al. 2013, Bechtold et al. 2008) and others found a positive relationship (Stirling and Stratton 2012). Observational studies also support a positive relationship. JD06 found a relatively strong positive relationship between congestus ERs and low-level (2-4 km) RH (R^2 = 0.2) and mid-level (5-7 km) RH (R^2 = 0.18), and Lu et al. (2018) found a strong positive relationship with RH in 8 shallow clouds (R = 0.8). We do not find a strong correlation with RH in the cloud layer (4-7 km for congestus, R^2 = 0.003) or with low-level (2-4 km) RH (R^2 = 0.036). However, our results support the qualitative (visual) results of the other observational studies of a positive correlation between ER and RH (Figure 11d). The reason for this relationship is not clear. Lu et al. (2018) hypothesize three different mechanisms explaining the positive relationship, including

a relationship with entrainment through the dependence of buoyancy and updraft velocity on RH. However, no obvious physical explanation is available for the negative relationship found in some LES and used in parameterizations.

We also evaluate relationships with environmental variables explored by JD06 that have not been tested with LES nor are typically used in GCM parameterizations, specifically the relationships between entrainment and CAPE, shear, and CIN. Given geographic differences between the maritime tropical congestus observed by JD06 and the continental tropical clouds of the Amazon, we do not necessarily expect perfect agreement. Any difference in results from each study could suggest a difference in the environmental drivers of entrainment rate and convective forcing mechanisms between two different locations due to oceanic convection observed in Nauru compared to continental convection in Brazil. In addition, the GoAmazon dataset contains nearly five times the amount of congestus clouds as the JD06 study.

We do not observe a relationship between entrainment and the must unstable (MU) and lowest 100 mb mixed layer (ML) CAPE in the lowest 5 km. Entrainment is slightly more correlated with ML-CAPE ($R^2 = 0.031$, Figure 11e) than MU-CAPE ($R^2 = 0.016$). This does not agree with the results of JD06 who found a larger correlation with low-level CAPE ($R^2 = 0.12$). The difference could be due to differing climates (continental vs. oceanic) that the congestus formed in.

In agreement with JD06, we find negligible relationships ($R^2 < 0.1$) with the average shear from the surface to 700 mb and CIN. We also observe no relationships with ELR in the cloud layer (3-6 km for congestus), vertical integral of moisture convergence, and large-scale vertical velocity at 700 mb. A few (6) congestus clouds have an entrainment rate larger than 3 standard deviations away from the mean. When these data points are removed from the analysis,

the correlations between entrainment and cloud thickness, cloud size, and buoyancy slightly improve. The relationships with the rest of the variables either weaken or remain relatively the same.

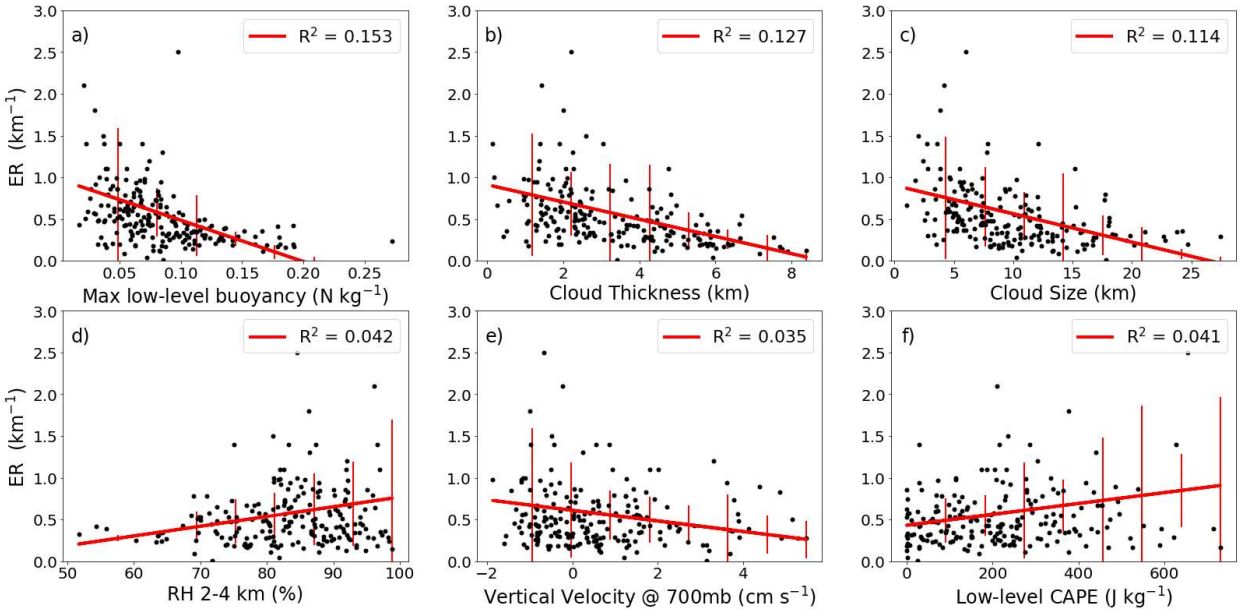

Figure 11: Entrainment versus several environmental and cloud variables in congestus clouds. The error bars represent the standard deviation of entrainment in appropriately sized bins.

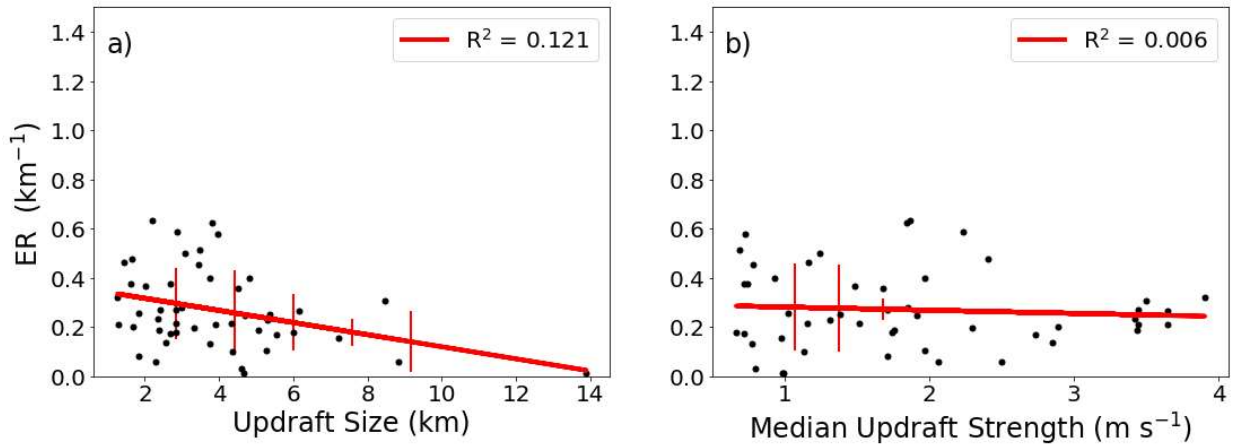

Figure 12: ER vs updraft horizontal size (a) and median strength (b) in the 37 congestus cases with a visually identifiable, vertically coherent updraft.

Because the sample size for the shallow clouds is small, it is difficult to make any robust conclusions about the behavior of entrainment in these clouds. Shallow cloud ERs have the strongest relationship with RH in the lowest 2 km ($R^2 = 0.42$). This relationship is positive (Figure 13d), like the congestus and other observational studies of entrainment in shallow clouds (Lu et al. 2018, Kirshbaum and Lamer 2020), but opposite the results of LES (de Rooy et al. 2013). The moderate correlations with cloud size ($R^2 = 0.12$) and low-level ML-CAPE ($R^2 = 0.12$) may be due to the lack of data points, since the plots show considerable scatter (Figure 13c, f). ELR in the cloud layer (1-3 km for shallow), vertical velocity, and moisture convergence have $R^2 < 0.1$. The strong positive correlation with shear ($R^2 = 0.261$) seems spurious, although entrainment could be related to shear-generated turbulence in weakly forced convective clouds (shallow clouds). Despite the strong relationships with cloud thickness and maximum buoyancy in the lowest 5 km in congestus clouds, ER for out limited number of shallow clouds do not exhibit any obvious dependence on these variables.

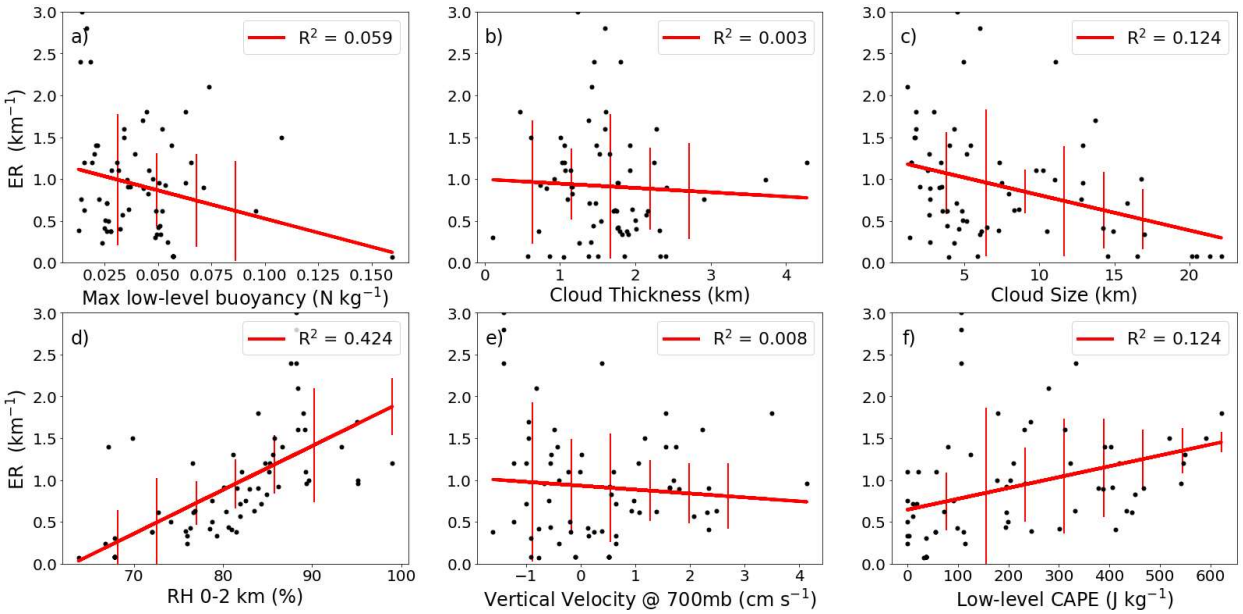

Figure 13: Same as Figure 11, but for shallow clouds.

Table 2: Linear correlation coefficient of entrainment rate and environmental and cloud variables for both shallow and congestus. The results of the "good" cases as well as the "better" cases (parenthesis) are presented and compared to JD06

ER vs...	Shallow R^2	Congestus R^2	JD06 R^2
	N=67 (n=20)	n=415 (n=210)	n=67
RH in the cloud layer	0.208 (0.002)	0.016 (0.003)	0.18
RH (2-4 km)	0.539 (0.056)	0.057 (0.042)	0.20
MU-CAPE in the lowest 5 km	0.078 (0.006)	0.0003 (0.016)	0.12
ML-CAPE in the lowest 5 km	0.124 (0.0003)	0.008 (0.041)	
Shear	0.0006 (0.261)	0.002 (0.007)	0.002
Max buoyancy	0.059 (0.015)	0.137 (0.153)	0.19
CIN	0.014 (0.004)	0.0003 (0.011)	0.03
ELR	0.037 (0.015)	0.0001 (0.012)	
Vertical Velocity at 700mb	0.010 (0.040)	0.015 (0.035)	
Moisture Convergence	0.011 (0.047)	0.001 (0.025)	
Cloud size	0.124 (0.070)	0.086 (0.115)	
Cloud thickness	0.003 (0.106)	0.122 (0.127)	
Average ER	0.914 (1.20)	0.478 (0.584)	
		n=37	
Updraft Size		0.12	
Updraft Speed		0.006	

The results were further broken down between the wet and dry season to see if different variables have important impacts in different seasons. Congestus and shallow cumulus clouds are present 8.9% and 27.9% of the time in the wet season, respectively, which is much higher than the dry season (2.8% and 16.8% of the time, respectively) (Giangrande et al. 2017). Our GoAmazon dataset contains 164 wet season, 127 dry season, and 123 transition season congestus, and 34 wet season, 19 dry season, and 14 transition season shallow clouds.

As mentioned earlier, 6 congestus clouds have entrainment rates larger than 2 km^{-1}, which is more than 3 times the standard deviation (σ) away from the mean. Each of these outlier clouds occurs in the wet season so in order to accurately compare ER values and relationships between the wet, dry, and transition seasons, these unphysical outliers were removed from the statistical analysis. These points do not appear to add any information to our dataset and are likely due to uncertainties in the method (e.g. unrepresentative initial parcel, large variations in the vertical thermodynamic profile, thermodynamic profile contamination from prior convection).

The average congestus entrainment rates are nearly the same in the dry (0.54 km^{-1}), wet (0.53 km^{-1}), and transition seasons (0.46 km^{-1}) (Table 3). The shallower CTHs and smaller mid-level RHs in the dry season have offsetting effects on the ER and therefore, the ER does not change much between the seasons. Shallow clouds have a slightly larger entrainment in the dry season (1.38 km^{-1}) than in the wet season (1.1 km^{-1}), although the number of low clouds in each category is insufficient to establish much in the way of a robust relationship. The variables with the largest seasonal cycle are shown in Table 3. Low mid-level RH, enhanced buoyancy and shear, and fewer, less organized cases characterize the dry season. For most of the variables, the entrainment correlations are the same and small in each season. Cloud size and maximum low-level buoyancy are more strongly correlated with entrainment in the dry season (Figure 14a,b). Cloud thickness is slightly more correlated with entrainment in the wet season (Figure 14c). Low-level CAPE and moisture convergence also have slightly larger R^2 in the wet season (not shown). The stronger correlations in the dry season may be explained by a better estimation of entrainment in the dry season. The dry season has a lower cloud frequency and therefore the

thermodynamic profile has less contamination due to other cloud or deep convective events, making the bulk-plume method a more accurate approach.

For shallow clouds, we observe so few cases in each season that it is uncertain if the observed relationships are meaningful. We find that low-level CAPE, ELR, shear, size, and vertical velocity are much more correlated with entrainment in the dry season. RH (0-2 km) and buoyancy are slightly more correlated with entrainment in the wet season (not shown). More observations of shallow clouds are needed to confirm these relationships.

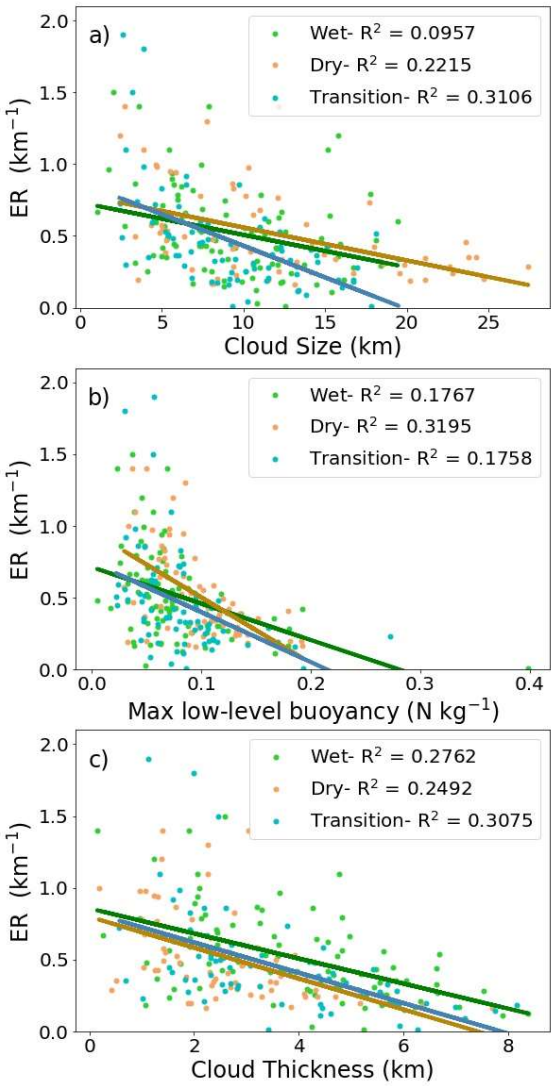

Figure 14: Entrainment vs cloud size (a), maximum buoyancy in the lowest 5 km (b), and cloud thickness (c) during the wet (green), dry (orange), and transition (blue) seasons.

Table 3: Mean values of several variables in each the dry, wet, and transition season. These are the variables with the largest seasonal differences.

	Dry (n=63)	Wet (n=74)	Transition (n=64)
ER	0.526	0.538	0.459
RH (4-7 km) (%)	50.8	76.6	66.5
CIN (J kg^{-1})	-76.8	-50.8	-68.9
Shear (cm s^{-1})	0.35	0.19	0.23
Low-level CAPE (J kg^{-1})	216	201	228
Low-level buoyancy (N kg^{-1})	0.097	0.074	0.081
Cloud size (km)	11.4	9.2	8.9

4.2.2 Regression Trees and Random Forests

As described previously, entrainment rate is likely not a simple linear function of a number of independent variables, so it is natural to explore more advanced statistical approaches to supplement the linear regression analysis. Regression trees for shallow and congestus clouds predict the variables with the largest effect on entrainment rates by grouping data with similar values of explanatory variables. Each group/node of the trees contains observations which are as homogenous as possible.

The optimal regression tree for the "better" congestus clouds is shown in Figure 15. The first tree split is made by separating the observations based on cloud thickness. There are slightly more cases with thickness greater than ~3000 m (54%) than less than ~3000 m (46%). The cases with the smaller thickness have a larger average entrainment rate (0.45 km^{-1}, Figure 15 Box #3) than those with large thickness (0.27 km^{-1}, Figure 15 Box #2). This negative relationship is consistent with the linear model results and LES scaling (Siebesma et al. 2003). The observations with large thickness (> ~ 3 km) are then split by their RH and those with smaller thickness (< ~ 3 km) are split by their large-scale vertical velocity. The group which contains observations with small thickness and large vertical velocity yield the largest average ER (0.65 km^{-1}, Figure 15

Box #7), but few cases fall into this category. However, the group which contains observations with small thickness and small vertical velocity represents a more substantial portion of the data and also has above average ER (0.41 km^{-1}, Figure 15 Box #6). The observations with large thickness and RH less than 80% produce the smallest ERs (0.23 km^{-1}, Figure 15 Box #4). Almost half of the observations fall into this category. The positive relationship between ER and RH is again shown in the regression tree results, but the relationship is stronger in the regression tree analysis than the linear regression analysis, since RH is one of the top three explanatory variables but had a small R^2 value. The regression tree analysis also suggests a positive relationship with the large-scale vertical velocity, which is not apparent from the linear regression analysis. The reason for the lack of correlation between entrainment and vertical velocity and RH may be because these variables are not independent. For example, the relationship between entrainment and vertical velocity is strongest in clouds with small thickness, indicating that the relationship may be dependent on both cloud thickness and vertical velocity. The root mean square error (RMSE) between the model predicted and observed data is 0.35 km^{-1}, giving it some statistical predictive power. This model shows that the variables which account for the entrainment variability are thickness, RH, and large-scale vertical velocity.

The shallow cloud regression tree results are shown in Figure 16. The observations are split only by the low-level RH. The majority of cases (58%) have low-level RH less than 84% and small ER (0.53 km^{-1}). The remaining cases with larger RH (>84%) have a much higher average entrainment rate (1.5 km^{-1}). A strong positive relationship with RH was also shown in the linear regression analysis and in several other observational studies (e.g. Lu et al. 2018). The model predicted and observed data has an RMSE of 0.43 km^{-1}, and therefore, the model cannot

alone predict entrainment rates. More data is needed to verify and make conclusions about the meaning of the relationships in the shallow clouds.

Random forests, an ensemble of regression trees, add more randomization and diversity to single regression trees, and therefore, are more robust against overfitting, reduce biases, and tend to be more accurate (Breiman 2001). The predictor variables are analyzed by their "importance" to the dependent variable (entrainment rate in this case), which is the reduction of the sum of squared error when that variable is used in a split, averaged over all trees in the forest. The results of the random forest model show that the cloud size, thickness, maximum low-level buoyancy, and vertical velocity have the most importance in determining entrainment in both shallow and congestus (Figure 17). Shear, RH, moisture convergence, ELR, and CAPE have a

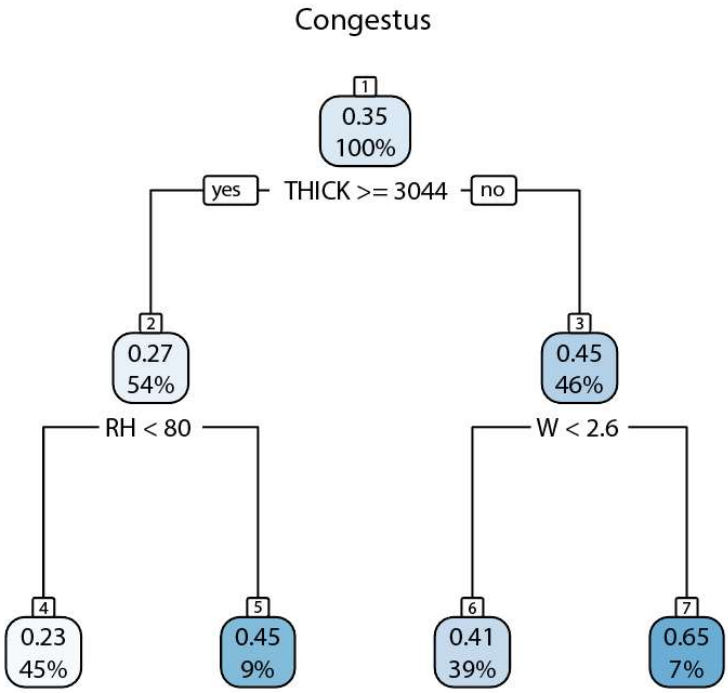

Figure 15: Regression tree indicating the variable splits for congestus entrainment rates. The top number is the average entrainment in the group and the bottom number is the percent of total observations that are in that group.

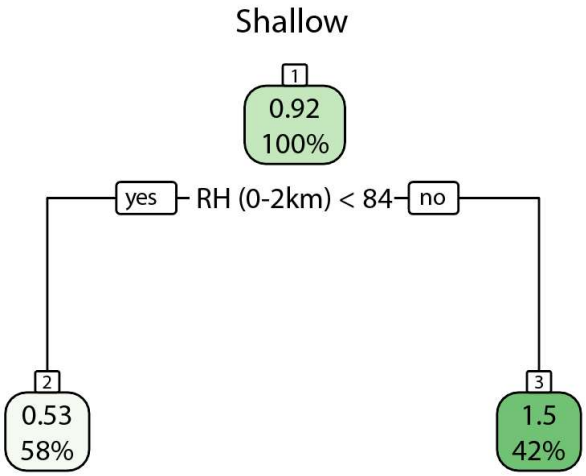

Figure 16: Same as Figure 15 but for shallow entrainment rates.

very small impact on ER. The relationship between cloud thickness is again apparent in this analysis. The most important variable is cloud size, which had a moderate linear R^2 value. Vertical velocity did not have a high linear R^2, but the regression tree and random forest analyses suggest a possible relationship with ER. Maximum low-level buoyancy had a relatively high linear R^2 value and is the second most important variable in the random forest model. The random forest model explains 45% of the variance in both congestus and shallow entrainment rates. The RMSE between the observed (testing data) and model predicted entrainment rates is 0.43 km^{-1} for congestus and 0.34 km^{-1} for shallow clouds. Though this does give evidence for some predictability, other factors are contributing to variability in entrainment rates besides those used in this study (discussion on potential sources of variability in section 5).

We also use a random forest to evaluate the seasonal differences of the entrainment relationships in congestus. The shallow cumulus have too few observations in each season to perform a random-forest analysis for each. The relative importance of each variable in each season is shown in Figure 18. In agreement with the linear analysis, cloud thickness is more important in the wet season. CAPE is also slightly more important in the wet season. Cloud size

is somewhat more important in the dry season, in agreement with the linear analysis, but not as apparent. The linear analysis also found a stronger relationship between entrainment and buoyancy in the dry season, and the random forest confirms this, showing a much stronger relationship in the dry season than the wet. The linear analysis did not suggest a seasonal difference in the relationship with vertical velocity, but the random forest shows vertical velocity with larger importance during the dry season than the wet. RH has consistent importance in the wet and dry season but is much more important in the transition season. These results, along with the linear regression results, suggest that entrainment could have different dependencies in different seasons, but the reasons for the different dependencies are unknown. We speculate that these differences could be due to more organized convection in the wet season than the dry or differences in the convective forcing mechanisms (i.e. mesoscale variability).

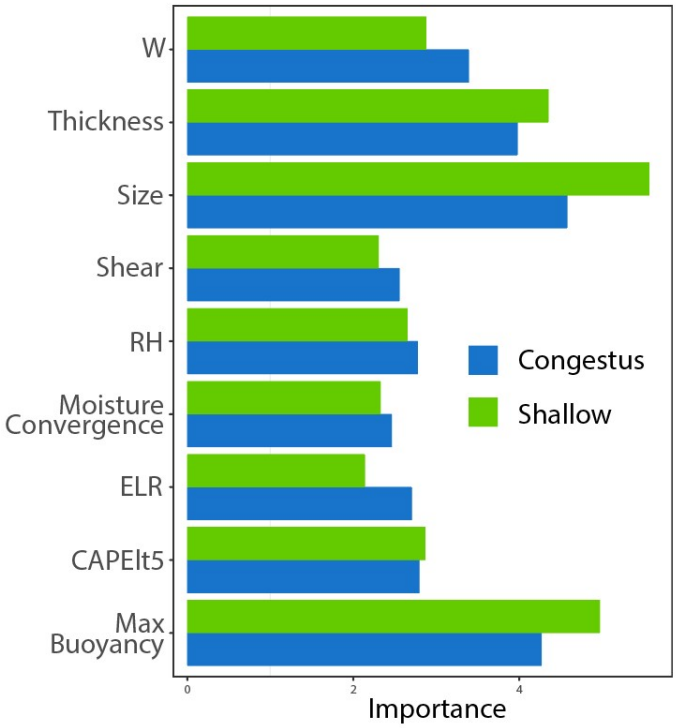

Figure 17: The importance of each cloud and environmental variable to entrainment as found by the random forest model. Congestus results are shown in blue and shallow results are in green.

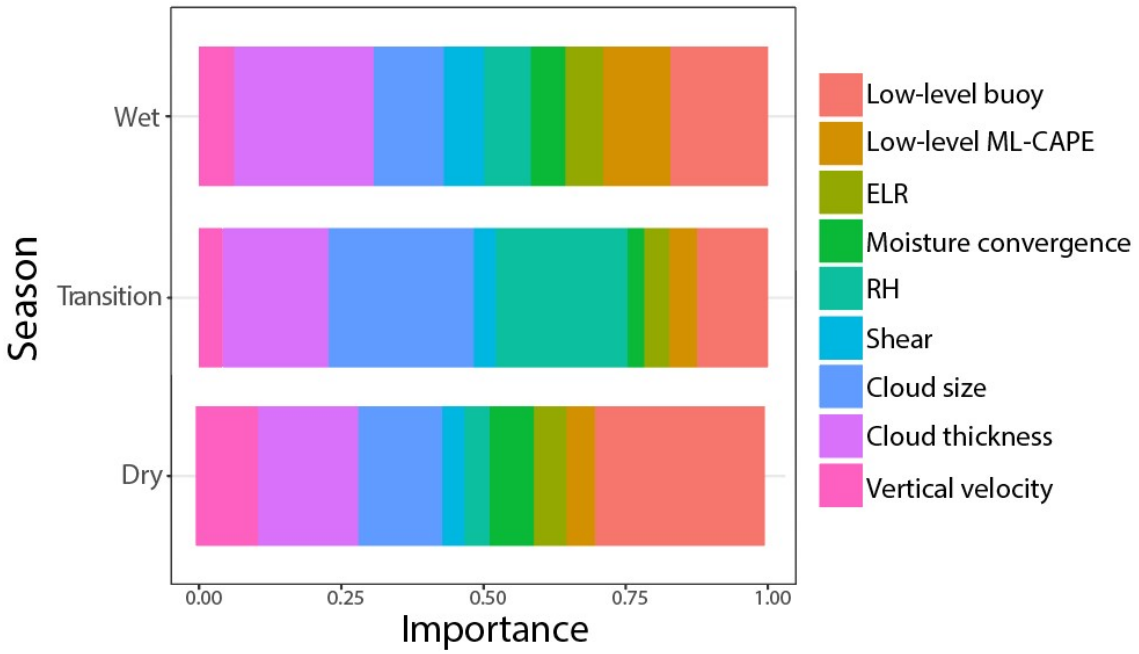

Figure 18: The random forest results of the relative importance of each explanatory entrainment variable in each season for congestus clouds.

4.3 *Uncertainty in entrainment rate calculations*

Uncertainty estimates in entrainment rate calculations are calculated by applying the standard error propagation techniques (Taylor 1982) to the instrument and retrieval uncertainties. Uncertainty in CTH can arise from a lack of WACR or RWP sensitivity, yielding an underestimate of CTH. This lack of sensitivity is a particular problem for the RWP, since the instrument is rather insensitive to cloud-size drops. We assume the minimum uncertainty in CTH is likely the size of a range gate, 200 m and 42 m for the RWP and WACR, respectively. We add and subtract 200 m to each cloud in the campaign and calculate the resulting entrainment rate for each cloud. Underestimating CTH by 200 m overestimates the average ER of the campaign by 0.05 km^{-1}, an 8.1% change. Qualitatively this makes sense since a higher CTH requires a smaller entrainment value. Similarly, overestimating CTH by 200 m underestimates the average ER by 0.07 km^{-1}, a 14.5% change. The changes in ER are not symmetric when the uncertainty is added and subtracted so we use the average magnitude change of all ER changes as the uncertainty in

entrainment due to CTH uncertainty, 0.06 km^{-1} (11.3%). When only the "better" cases are considered, the average ER uncertainty for both adding and subtracting the CTH uncertainty is 0.08 km^{-1} (15%).

The entrainment uncertainty due to cloud top uncertainty and due to thermodynamic retrieval uncertainty are about the same magnitude. Table 1 of the appendix shows the ER using all possible combinations of adding and subtracting the temperature and moisture uncertainty profiles for a single, ideal case. The ER uncertainty due to sounding, MWRP, and MWR measurement uncertainties is found by averaging the magnitudes of the four uncertainties, resulting from the four possible combinations of adding and subtracting the temperature and moisture uncertainty profiles, 0.065 km^{-1}. The largest uncertainty comes from the addition of both the temperature and moisture uncertainties. The ER increases by 0.075 km^{-1}, which is qualitatively expected from a parcel with greater buoyancy. The ER changes more when the moisture uncertainty is applied than the temperature. This is likely not due to the buoyancy differences in the parcel controlling the entrainment rate, but due to the difference in the environmental air entrained into the parcel.

We combine the ER uncertainties due to CTH and thermodynamic profile uncertainties using the sum of squares to find the final entrainment rate uncertainty. This value is 0.088 km^{-1} for the "good" cases and 0.102 km^{-1} for the "better" cases.

4.4 *Sensitivity tests*

We test the sensitivity of our entrainment rates to the assumptions we use in the bulk-plume model and how we determine the environmental correlations. We have assumed that parcels originated at the surface and ascended pseudoadiabatically, and that the environmental profiles were representative of the environments that the clouds grew in. The entrainment

correlations were done separately for shallow cumulus and congestus clouds, assuming that shallow cumulus had CTH between 1 and 3 km and congestus had CTH between 3 and 9 km.

Instead of using a surface-based parcel, we assume the parcel initial conditions are representative of a mixed-layer of varying depths. Figure 19 shows the differences of entrainment rates between a surface-based parcel and a mixed-layer average over the lowest 1000, 500, and 100 m. Surface-based ERs are larger than the 1000 m and 500 m ML ERs for the majority of cases (68%, 60%, respectively). Surface-based parcels are more buoyant and are expected to have larger ER, but surprisingly the difference is relatively small. The largest changes are from the 1000 m and 500 m ML parcels, which have an average difference of 0.048 (10 %) and 0.050 km^{-1} (10.5%), respectively. The 100 m ML difference is much smaller (5.1%). Our choice of initial parcel properties yeilds a magnitude of uncertainty similar to the CTH and thermodynamic profile uncertainties. However, regardless of the choice of initial parcel origin, the variables with the largest correlations with entrainment do not change for both shallow cumulus and congestus (not shown).

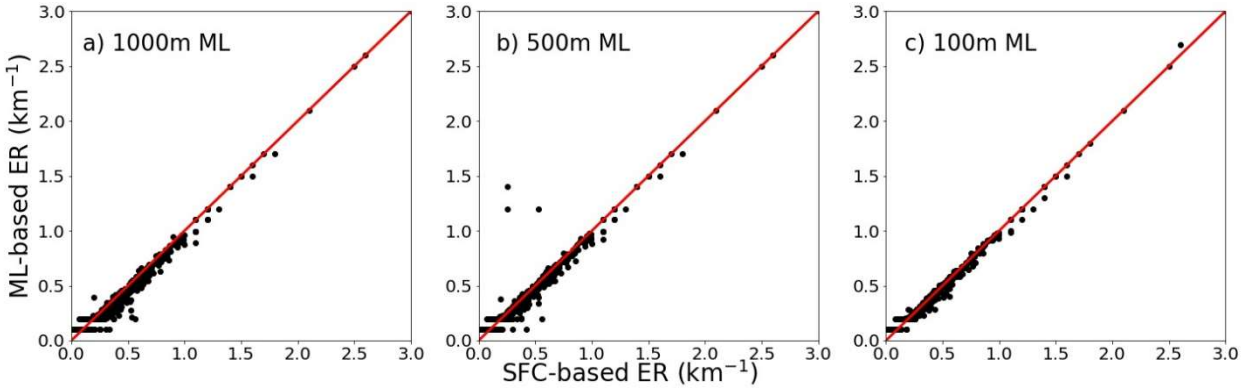

Figure 19: Mixed layer parcel entrainment rates versus the surface-based parcel entrainment rates for a 1000 m mixed layer (a), 500 m mixed layer (b), and 100 m mixed layer (c).

We also compare our best estimate ER and environmental variable correlations to the ER correlations using only the sounding, but only the cases that have the nearest prior sounding

within 3 hours and 1 hour. If the corrections are accurate and improve the thermodynamic profile, they should produce similar correlations to the cases where the sounding is within an hour of the cloud observation and is therefore an accurate representation of the thermodynamic environment. Table 4 shows the results for congestus and Table 5 shows them for shallow. The correlations between entrainment and each environmental variable are similar for the corrected cases and the cases with a sounding within 1 and 3 hours for congestus. Shallow cumulus entrainment rates are more correlated with buoyancy and cloud thickness in the cases that use soundings than those that use the MWRP correction. This shows that we are not missing a strong correlation between the ER and environmental variables because of the low temporal resolution of the soundings, assuming we apply the MWRP correction.

Table 4: R^2 values of entrainment with the environmental variables for the "better" congestus using the MWRP correction compared to cases using sounding values within 3 hours and 1 hour.

ER vs…	MWRP Corrected R^2 (n = 210)	Sounding within 3 hours (n = 348)	Sounding within 1 hour (n = 158)
RH in the cloud layer	0.003	0.015	0.020
ML-CAPE in the lowest 5 km	0.016	0.005	0.018
Shear	0.007	0.0002	~ 0
Max low-level buoyancy	0.157	0.176	0.182
ELR	0.012	0.0004	~ 0
Thickness	0.133	0.146	0.149

Table 5: Same as Table 4 but for shallow entrainment correlations.

ER vs...	MWRP Corrected R^2 (n = 67)	Sounding within 3 hours (n = 48)	Sounding within 1 hour (n = 14)
RH in the cloud layer	0.208	0.056	0.003
ML-CAPE in the lowest 5 km	0.124	0.084	0.094
Shear	0.0006	0.017	0.015
Max low-level buoyancy	0.059	0.178	0.559
ELR	0.037	0.004	0.069
Thickness	0.003	0.023	0.180

We also test the sensitivity of our results to our definition of shallow and congestus. Table 6 shows the ER environmental correlations for shallow CTHs less than 4 km and congestus CTHs between 4 and 9 km. The shallow ER correlations weaken considerably, likely because the sample size was drastically increased. Most of the congestus correlations also weaken. The largest change is the correlation with RH in the cloud layer and shear, which both increase when congestus are defined as CTH 4-9 km. This comes at the expense of the shallow RH and shear correlations, which decrease as the definition changes. The other variables, however, do not have much sensitivity to the CTH definitions of shallow and congestus.

Table 6: Entrainment correlations with environmental variables for different congestus and shallow CTH definitions. "Good" shallow clouds and "better" congestus clouds are used.

ER vs...	Shallow (1-3km) (n = 67)	Shallow (1-4km) (n = 220)	Congestus (3-9km) (n = 210)	Congestus (4-9km) (n = 142)
RH in the cloud layer	0.208	0.07	0.003	0.029
CAPE in the lowest 5 km	0.124	0.09	0.016	0.015
Shear	0.0006	0.006	0.007	0.031
Max buoyancy	0.059	0.057	0.157	0.142
Size	0.037	0.059	0.127	0.041
Thickness	0.003	0.011	0.133	0.047

5 Conclusions and Discussion

Shallow cumulus and cumulus congestus clouds are not simulated well in GCMs, despite their importance to tropical dynamics (Williams and Tselioudis 2007, Nam et al. 2012). Convective parameterizations, including how entrainment is represented, are a large source of uncertainty in GCMs. Entrainment-rate closures have largely been formulated from LES, and few observational entrainment studies exist. The purpose of this study was to estimate observational entrainment rates in shallow cumulus and cumulus congestus during the GoAmazon 2014/5 field campaign. We expand on the methods of JD06 to calculate entrainment rate by including additional sensors to determine the best-estimate of CTH and representative thermodynamic profile. This study contrasts with JD06 through the addition of multiple sensors, a greater number of congestus cases in our analysis, a different meteorological environment (tropical continental), and a particular focus on uncertainty propagation. We evaluate common entrainment closures supported by LES using standard linear correlation analysis but also machine-learning models that embrace the nonlinearity and covariability inherent in the relationships among the different variables.

A multi-sensor approach is employed to give the best estimates of CTH and thermodynamic state. We use a combination of the WACR and RWP reflectivities to find a best estimate of CTH. The WACR attenuates in the presence of precipitation, which gives an underestimate of CTH that would result in a subsequent overestimate of ER if used in out algorithm. The RWP is less sensitive to cloud droplets but is sensitive to the precipitation droplets and does not attenuate as much. In some cases, the WACR CTH is more than 5 km lower than the RWP CTH. Use of the improved CTH estimates results in a decrease in the retrieved ERs by an average of 0.078 km^{-1} (13.6%). These results strongly suggest that future

field campaigns use the RWP in conjunction with cloud radars to obtain accurate macrophysical cloud properties, especially when sampling clouds with larger hydrometeors.

Our best estimate of the thermodynamic profile uses the MWRP and MWR retrievals to improve the temporal resolution of the sounding profiles and provide a profile more representative of the environment in which the cloud grew. The nearest prior sounding generally underestimates the temperature and moisture, since the majority of the clouds occur in the afternoon. The more representative thermodynamic profile changes the entrainment rates by 0.0995 km^{-1} (25%). The ER estimation is highly sensitive to changes in the boundary layer thermodynamics, and therefore representative thermodynamics at the time of the cloud are imperative to estimating ERs. Supplementing relatively infrequent soundings with high-temporal-resolution remote-sensing retrievals to improve observational estimates of the thermodynamic profiles is highly desirable.

The main findings of our entrainment rate correlation analysis are summarized below:

- We find entrainment rates ranging from 0.19 to 0.94 km^{-1} with an average of 0.57 ± 0.088 km^{-1} in 415 congestus clouds, which are moderately correlated with the maximum buoyancy in the lowest 5 km, cloud thickness, and cloud size. These correlations are quantified by the linear regression, regression tree, and random forest analysis. The machine-learning models also suggest a nonlinear relationship with the large-scale vertical velocity at 700 mb.
- We find entrainment rates ranging from 0.63 to 1.7 km^{-1} with an average of 1.2 ± 0.088 km^{-1} in 67 shallow cumulus clouds, which have a strong relationship with the low-level (0-2 km) RH, and moderate relationships with low-level CAPE and cloud size, although we are cautious about these results given the small number of shallow cumulus observed.

- Our linear analysis and random forest results show a difference in entrainment rate relationships between the wet, dry, and transition seasons. Both analyses showed that entrainment depends on cloud size, buoyancy, and vertical velocity more in the dry season than in the wet. Entrainment tends to be best associated with cloud thickness and low-level CAPE in the wet season, whereas RH is a more important factor during the transition season. We speculate that these differences could be due to more organized convection in the wet season than the dry or mesoscale variability, but more analysis needs to be done to understand the differing seasonal dependencies.

Our congestus correlations differ from those of JD06, who found that entrainment most depended on low-level CAPE and RH in maritime congestus, whereas we find these variables explain only a small portion of the variance in entrainment. The difference in results between these studies suggests a difference in the environmental drivers of entrainment rate across different regimes. Continental convection forcings may influence the entrainment rates and partially explain the difference in ER sensitivities between oceanic and continental climates. These forcings, unique to continental locations, including sea or river breezes, urban heat island effects, and aerosols, may also contribute to the lack of sensitivity of entrainment to the explanatory variables.

The shallow cumulus entrainment rates and correlations agree with other recent observational studies of entrainment in continental shallow cumulus, showing a strong dependence on RH (Lu et al. 2018, Kirshbaum and Lamer 2020). However, LES suggests a negative relationship. More research needs to be done to assess the reason for the sign differences in the relationship between entrainment rates estimated from observations and LES,

which we speculate may at least in part arise from the differences in how the entrainment rate is defined and calculated.

Our analysis gives some observational support for several of the entrainment closures supported by LES, but the correlations between entrainment and the environmental and cloud variables are fairly weak and do not fully explain the variability in entrainment rate. The remaining variance could be explained by the small spatial and temporal scales used to represent the thermodynamic profile, observation uncertainties, and limitations of the bulk-plume method. Though we have improved the thermodynamic profile and CTH estimates, observational limitations and uncertainties from the retrievals remain, which we have worked to quantify. For example, the MWRP and MWR retrievals improved the temporal resolution of our thermodynamic profiles but have coarse vertical resolution. The Amazon region has considerable mesoscale variability, including the continental effects mentioned above as well as cold pools or dry/moist layers resulting from prior convection, which may all impact the entrainment rates. We also only sample the clouds directly above the radar. Therefore, the radar observations and their entrainment values may not be representative of the total cloud population over a larger area. Further, in the majority of the cases, we rarely observe the center of the updraft, and therefore suffer from chording biases. We likely underestimate the true maximum CTH associated with the largest updraft, and consequently overestimate the entrainment rate. The magnitude of these biases is unknown and left for a future study. Limitations of the theoretical assumptions of the bulk-plume method include representing convection by an idealized plume undergoing continuous, linear entrainment with height. Convection that is more transient than steady may be better represented by a bubble entraining at cloud top (Yano 2014). Furthermore, entrainment may not be constant with height. Several studies have estimated the vertical

dependence of entrainment and found that entrainment is maximum at cloud base and decreasing above (Lin 1999, Lu et al. 2012, de Rooy et al. 2013). However, JD06 tested the sensitivity of their results to height-varying entrainment rates and found little change in their results.

Future work should further explore the seasonal entrainment dependencies and the nature of the dependencies but would require additional field deployments or long-term LES of the Amazon environment. In addition, it would be beneficial to compare the observations with LES simulations of GoAmazon clouds and entrainment rates, and further explore the role of nonlinear relationships and interactions between variables in predicting entrainment rates and the mechanisms behind the relationships.

Appendix

Thermodynamic uncertainty estimates

Table 1: The ER results from adding and subtracting the temperature and moisture uncertainties to an ideal thermodynamic profile in all possible combinations. The resulting ERs are compared to the ideal ER, and the changes are determined to be the uncertainty in ER.

Arbitrary CTH (km)	6		
ER (km^{-1})	0.283		
Profile change	ER (km^{-1})	ER change (km^{-1})	% ER change
Add T, Add q	0.358	0.075	26.5
Add T, Sub q	0.215	-0.068	-24.0
Sub T, Add q	0.347	0.064	22.6
Sub T, Sub q	0.231	-0.052	-18.4
Average		0.065	22.9
Add T	0.280	-0.003	-1.1
Sub T	0.286	0.003	1.1
Add q	0.353	0.07	24.7
Sub q	0.224	-0.059	-20.8

References

Albrecht, B. A., 1984: A Model Study of Downstream Variations of the Thermodynamic Structure of the Trade Winds. *Tellus A*, **36A**, 187-202.

Bechtold, P., E. Bazile, F. Guichard, P. Mascart, and E. Richard, 2001: A mass-flux convection scheme for regional and global models. *Q. J. Royal Meteorol. Soc.,* **127**, 869-886.

Bechtold, P., M. Köhler, T. Jung, F. Doblas-Reyes, M. Leutbecher, M. J. Rodwell, F. Vitart and G. Balsamo, 2008: Advances in Simulating Atmospheric Variability with the ECMWF Model: From Synoptic to Decadal Time-Scales. *Q. J. Royal Meteorol. Soc.,* **134**, 1337-1351.

Borque, P., P. Kollias, and S. Giangrande, 2014: First Observations of Tracking Clouds Using Scanning ARM Cloud Radars. *J. Appl. Meterol. Clim.,* **53,** 2732-2746.

Brast, M., R. A. J. Neggers, and T. Heus, 2016: What Determines the Fate of Rising Parcels in a Heterogeneous Environment? *J. Adv. Model. Earth Syst*., **8**, 1674-1690.

Breiman, L., J. Friedman, C. J. Stone, and R. A. Olshen, 1984: *Classification and Regression Trees*, Wadsworth, Belmont, CA

Breiman, L.,2001: Random forests, *Mach. Learning*, **45**, 5–32.

Bretherton, C. S., J. R. McCaa, and H. Grenier, 2004: A New Parameterization for Shallow Cumulus Convection and Its Application to Marine Subtropical Cloud-Topped Boundary Layers. Part 1: Description and 1D Results. *Mon. Wea. Rev,* **132**, 864-882.

Cadeddu, M. P. and J. Liljegren, 2018: Microwave Radiometer Profiler (MWRP) Instrument Handbook.

Cadeddu, M. P., J. Liljegren, and D. D. Turner, 2013: The Atmospheric radiation measurement (ARM) program network of microwave radiometers: instrumentation, data, and retrievals. *Atmos. Meas. Tech.,* **6**, 2359–2372.

Cheng, C.-P. and R. A. Houze, 1979: The Distribution of Convective and Mesoscale Precipitation in GATE Radar Echo Patterns. *Mon. Wea. Rev,* **107**, 1370-1381.

Clothiaux, E. E., T. P. Ackerman, G. G. Mace, K. P. Moran, R. T. Marchand, M. A. Miller, and B. E. Martner, 2000: Objective Determination of Cloud Heights and Radar Reflectivities Using a Combination of Active Remote Sensors at the ARM CART Sites. *J. Appl. Meteor., **39**, 645-665.*

Cooper, W. A., S. G. Lasher-Trapp, A. M. Blyth, 2013: The Influence of Entrainment and Mixing on the Initial Formation of Rain in a Warm Cumulus Cloud. *J. Atmos. Sci.,* **70**, 1727-1743.

Dawe, J. T. and P. H. Austin, 2012: Statistical Analysis of an LES Shallow Cumulus Cloud Ensemble Using a Cloud Tracking Algorithm. *Atmospheric Chem. Phys.,* **12**, 1101-1119.

Del Genio, A.D., 2012: Representing the Sensitivity of Convective Cloud Systems to Tropospheric Humidity in General Circulation Models. *Surv. Geophys.*, **33**, 637-656.

de Rooy, W. C., P. Bechtold, K. Frohlich, C. Hohenegger, H. Jonker, D. Mironov, A. P. Siebesma, J. Teixeira, and J.-I. Yano, 2013: Entrainment and Detrainment in Cumulus Convection: An Overview. *Q. J. Royal Meteorol. Soc.,* **139**, 1-19.

Derbyshire, S. H., I. Beau, P. Bechtold, J.-Y. Grandpeix, J.-M. Piriou, J.-L. Redelsperger and P. M. M. Soares, 2004: Sensitivity of Moist Convection to Environmental Humidity. *Q. J. Royal Meteorol. Soc.,* **130**, 3055-3079.

Drueke, S., D. J Kirshbaum, and P. Kollias, 2019: Evaluation of Shallow-Cumulus Entrainment Rate Retrievals Using Large-Eddy Simulation. *J. Geophys. Res. Atmos.*, **124**, 9624-9643.

Feng, Zhe, and S. E. Giangrande, 2018: Merged RWP-WACR-ARSCL Cloud Mask and Cloud Type. Web. doi:10.5439/1462693.

Gaustad, K. L. and D. D. Turner, 2007: MWRRET Value-Added Product: The Retrieval of Liquid Water Path and Precipitable Water Vapor from Microwave Radiometer (MWR) Datasets.

Giangrande, S. E., S. Collis, J. Straka, A. Protat, C. Williams, and S. Krueger, 2013: A Summary of Convective-Core Vertical Velocity Properties Using ARM UHF Wind Profilers in Oklahoma. *J. Appl. Meteorol. Climatol.*, **52**, 2278-2295.

Giangrande, S. E., T. Toto, M. P. Jensen, M. J. Bartholomew, Z. Feng, A. Protat, C. R. Williams, C. Schumacher, and L. Machado, 2016: Convective Cloud Vertical Velocity and Mass-Flux Characteristics from Radar Wind Profiler Observations During GoAmazon2014/5. *J. Geophys. Res. Atmos.*, **121**, 12891–12913.

Giangrande, S. E., Z. Feng, M. P. Jensen, J. M. Comstock, K. L. Johnson, T. Toto, M. Wang, C. Burleyson, N. Bharadwaj, F. Mei, L. A. T. Machado, A. O. Manzi, S. Xie, S. Tang, M. A. F. Silva Dias, R. A. F de Souza, C. Schumacher, and S. T. Martin, 2017: Cloud Characteristics, Thermodynamic Controls and Radiative Impacts During the Observations and Modeling of the Green Ocean Amazon (GoAmazon2014/5) Experiment. *Atmos. Chem. Phys*., **17**, 14519–14541.

Giangrande, S. E., D. Wang, and D. B. Mechem, 2020: Cloud Regimes Over the Amazon Basin: Perspectives from the GoAmazon2014/5 Campaign. *Atmos. Chem. Phys*., **20**.

Grant, A. L. M. and A. R. Brown, 1999: A Similarity Hypothesis for Shallow-Cumulus Transports. *Q. J. Royal Meteorol. Soc.,* **125**, 1913-1936.

Haynes, J. M., T. S. L'Ecuyer, G. L. Stephens, S. D. Miller, C. Mitrescu, N. B. Wood, and S. Tanelli, 2009: Rainfall Retrieval Over the Ocean with Spaceborne W-band Radar. *J. Geophys. Res,* **114**.

Heus, T., G. van Duk, H. J. J. Jonker, and H. E. A. Van den Akker, 2008: Mixing in Shallow Cumulus Clouds Studied by Lagrangian Particle Tracking. *J. Atmos. Sci.,* **65**, 2581-2597.

Holdridge, D., J. Prell, M. Ritsche, and R. Coulter, 2011: Balloon-Borne Sounding System (SONDE) Handbook.

Jensen, M. P. and A. D. Del Genio, 2006: Factors Limiting Convective Cloud-Top Height at the ARM Nauru Island Climate Research Facility. *J. Climate,* **19**, 2105-2117.

Johnson, R. H., T. M. Rickenbach, S. A. Rutledge, P. E. Ciesielski and W. H. Schubert, 1999: Trimodal Characteristics of Tropical Convection. *J. Climate,* **12**, 2397-2418.

Jorgensen, D. P., E. J. Zipser, and M. A. LeMone, 1985: Vertical Motions in Intense Hurricanes. *J. Atmos. Sci.,* **42**, 839–856.

Kain, J. S. and J. M. Fritsch, 1990: A One-Dimensional Entraining/Detraining Plume Model and Its Application in Convective Parameterization. *J. Atmos. Sci.,* **47**, 2784-2802.

Kirshbaum, D. and K. Lamer, 2020: Climatology of ShCu bulk entrainment at the SGP observatory. *ASR Science Team Meeting*. U.S. Department of Energy, remote web conference. https://www.orau.gov/2020armasr/presentations/Friday-Warm-Boundary/wblp-m2-Kirshbaum_shcu_entrainment.pdf.

Kollias, P., E. E. Clothiaux, B. A. Albrecht, M. A. Miller, K. P. Moran, and K. L. Johnson, 2005: The Atmospheric Radiation Measurement Program Cloud Profiling Radars: An Evaluation of Signal Processing and Sampling Strategies. *J. Atmos. Oceanic Technol.,* **22**, 930–948.

Kuhn, M. and K. Johnson, 2013: *Applied Predictive Modeling*. Springer.

Liljegren, J. C., B. M. Lesht, S. Kato, E. E. Clothiaux, 2001: Evaluation of Profiles of Temperature, Water Vapor, and Cloud Liquid Water from a New Microwave Radiometer. *Eleventh ARM Science Team Meeting Proceedings,* Atlanta, Georgia, March 19-23.

Lin, C., 1999: Some Bulk Properties of Cumulus Ensembles Simulated by a Cloud-Resolving Model. Part 1: Cloud Root Properties. *J. Atmos. Sci.,* **56**, 3724-3735.

Lin, C., 1999: Some Bulk Properties of Cumulus Ensembles Simulated by a Cloud-Resolving Model. Part 2: Entrainment Profiles. *J. Atmos. Sci.,* **56**, 3736–3748.

Lin, C. and A. Arakawa, 1997: The Macroscopic Entrainment Processes of Simulated Cumulus Ensemble. Part 1: Entrainment Sources. *J. Atmos. Sci.,* **54**, 1027-1043.

Lintner, B. R., D. K. Adams, K. A. Schiro, A. M. Stansfield, A. A. Amorim Rocha, and J. D. Neelin, 2017: Relationships Among Climatological Vertical Moisture Structure, Column Water Vapor, and Precipitation Over the Central Amazon in Observations and CMIP5 Models, *Geophys. Res. Lett.*, **44**, 1981-1989.
Lu, C., Y. Liu, S. S. Yum, S. Niu, and S. Endo, 2012: A New Approach for Estimating Entrainment Rate in Cumulus Clouds. *Geophys. Res. Lett.*, **39**, L04802.

Lu, C., C. Sun, Y. Liu , G. J. Zhang, Y. Lin, W. Gao, S. Niu, Y. Yin, Y. Qiu, and L. Jin, 2018: Observational Relationship Between Entrainment Rate and Environmental Relative Humidity and Implications for Convection Parameterization, *Geophys. Res. Lett.*, **45**, 13495-13504.

Luke, E. P. and P. Kollias, 2013: Separating Cloud and Drizzle Radar Moments during Precipitation Onset Using Doppler Spectra, *J. Atmos. Oceanic Technol.*, **30**, 1656–1671.

Luo, Z., G. Y. Liu, G. L. Stephens, and R. H. Johnson, 2009: Terminal Versus Transient Cumulus Congestus: A CloudSat Perspective, *Geophys. Res. Lett.*, **36**, L05808.

Martin, S. T., P. Artaxo, L. A. T. Machado, A. O. Manzi, R. A. F. Souza, C. Schumacher, J. Wang, M. O. Andreae, H. M. J. Barbosa, J. Fan, G. Fisch, A. H. Goldstein, A. Guenther, J. L. Jimenez, U. Pöschl, M. A. Silva Dias, J. N. Smith, and M. Wendisch, 2016: Introduction: Observations and Modeling of the Green Ocean Amazon (GoAmazon2014/5), *Atmos. Chem. Phys.*, **16**, 4785–4797.

Martin, S. T., P. Artaxo, L. Machado, A. O. Manzi, R. A. F. Souza, C. Schumacher, J. Wang, T. Biscaro, J. Brito, A. Calheiros, K. Jardine, A. Medeiros, B. Portela, S. S. de Sá, K. Adachi, A. C. Aiken, R. Albrecht, L. Alexander, M. O. Andreae, H. M. J. Barbosa, P. Buseck, D. Chand, J. M. Comstock, D. A. Day, M. Dubey, J. Fan, J. Fast, G. Fisch, E. Fortner, S. Giangrande, M. Gilles, A. H. Goldstein, A. Guenther, J. Hubbe, M. Jensen, J. L. Jimenez, F. N. Keutsch, S. Kim, C. Kuang, A. Laskin, K. McKinney, F. Mei, M. Miller, R. Nascimento, T. Pauliquevis, M. Pekour, J. Peres, T. Petäjä, C. Pöhlker, U. Pöschl, L. Rizzo, B. Schmid, J. E. Shilling, M. A. Silva Dias, J. N. Smith, J. M. Tomlinson, J. Tóta, and M. Wendisch, 2017: The Green Ocean Amazon Experiment (GoAmazon2014/5) Observes Pollution Affecting Gases, Aerosols, Clouds, and Rainfall over the Rain Forest. *Bull. Amer. Meteor. Soc.*, **98**, 981–997.

Masunaga, H. and Z. J. Luo, 2016: Convective and Large-Scale Mass Flux Profiles over Tropical Oceans Determined from Synergistic Analysis of a Suite of Satellite Observations, *J. Geophys. Res. Atmos.,* **121**, 7958-7974.

McFarlane, S. A., C. N. Long, and J. Flaherty, 2013: A Climatology of Surface Cloud Radiative Effects at the ARM Tropical Western Pacific Sites. *J. Appl. Meteorol. Climatol.*, **52**, 996-1013.

Mechem, D. B. and A. J. Oberthaler, 2013: Numerical Simulation of Tropical Cumulus Congestus During TOGA COARE. *J. Adv. Model. Earth Syst.,* **5**, 623-637.

Miller, M. A., Nitschke, K., Ackerman, T. P., Ferrell, W., Hickmon, N., and Ivey, M., 2016: The Atmospheric Radiation Measurement Mobile Facility, Chapter, AMS Monograph, The first 20 years of ARM.

Morton, B. R., G. I. Taylor, and J. S. Turner, 1956: Turbulent Gravitational Convection from Maintained and Instantaneous Sources. *Proc. R. Soc. Lon. A,* **234**, 1-23.

Nam, C., S. Bony, J.-L. Dufresne, and H. Chepfer, 2012: The "too few, too bright" Tropical Low-Cloud Problem in CMIP5 models. *Geophys. Res. Lett.,* **39**, L21801.

Neggers, R. A. J., A. P. Siebesma and H. J. J. Jonker, 2002: A Multiparcel Model for Shallow Cumulus Convection. *J. Atmos. Sci.,* **59**, 1655-1668.

Neggers, R. A. J., J. D. Neelin and B. Stevens, 2007: Impact Mechanisms of Shallow Cumulus Convection on Tropical Climate Dynamics. *J. Climate,* **20**, 2623-2642.

Paluch, I. R., 1979: The Entrainment Mechanism in Colorado Cumuli. *J. Atmos. Sci.,* **36**, 2467-2478.

Rauber, R., H. T. Ochs, III, L. Di Girolamo, S. Göke, and E. Snodgrass, 2007: Rain in (shallow) Cumulus Over the Ocean- the RICO Campaign, *Bull. Am. Meteorol. Soc.,* **88**, 1912-1928.

Riehl, H., T. C. Yeh, J. S. Malus, and N. E. La Seur, 1951: The North-East Trade of the Pacific Ocean. *Q. J. Royal Meteorol. Soc.*, **77**, 598–626.

Romps, D. M., 2010: A Direct Measure of Entrainment, *J. Atmos. Sci.,* **67**, 1908-1927.

Siebesma, A. P. and J. W. M. Cuijpers, 1995: Evolution of Parametric Assumptions for Shallow Cumulus Convection. *J. Atmos. Sci.,* **52**, 650-666.

Siebesma, A. P., C. S. Bretherton, A. Brown, A. Chlond, J. Cuxart, P. G. Duynkerke, H. Jiang, M. Khairoutdinov, D. Lewellen, C.-H. Moeng, E. Sanchez, B. Stevens and D. E. Stevens, 2003: A Large Eddy Simulation Intercomparison Study of Shallow Cumulus Convection. *J. Atmos. Sci.,* **60**, 1201-1219.

Steiner, M., R. Houze, S. Yuter, 1995: Climatological Characterization of Three-Dimensional Storm Structure from Operational Radar and Rain Gauge Data, *J. Appl. Meteorol,* **34**, 1978-2007.

Stephens, G. L. and N. B. Wood, 2007: Properties of Tropical Convection Observed by Millimeter-Wave Radar Systems. *Mon. Wea. Rev,* **135**, 821-842.

Stirling, A. J. and R. A. Stratton, 2012: Entrainment Processes in the Diurnal Cycle of Deep Convection Over Land, *Q. J. Royal Meteorol. Soc.,* **138**, 1135–1149.

Stull, R., 1985: A Fair-Weather Cumulus Cloud Classification Scheme for Mixed-Layer Studies. *Journal of Climate and Applied Meteorology, **24***, 49-56.

Squires, P., 1958: Penetrative Downdraughts in Cumuli. *Tellus,* **10**, 381-389.

Takahashi, H., Z. J. Luo, and G. L. Stephens, 2017: Level of Neutral Buoyancy, Deep Convective Outflow, and Convective Core: New Perspectives Based on 5 Years of CloudSat Data, *J. Geophys. Res. Atmos.*, **122**, 2958–2969.

Tang, S., S. Xie, Y. Zhang, M. Zhang, C. Schumacher, H. Upton, M. P. Jensen, K. L. Johnson, M. Wang, M. Ahlgrimm, Z. Feng, P. Minnis, and M. Thieman, 2016: Large-Scale Vertical Velocity, Diabatic Heating and Drying Profiles Associated with Seasonal and Diurnal Variations of Convective Systems Observed in the GoAmazon2014/5 Experiment. *Atmos. Chem. Phys.*, **16**, 14249–14264.

Taylor, J. R., 1982: *Introduction to Error Analysis: The Study of Uncertainties in Physical Measurements.* Mill Valley, Calif: University Science Books.

Turner, J. S., 1969: Buoyant Plumes and Thermals, *Annu. Rev. Fluid Mech*., **1**, 29–44.

Turner, D. D., T. R. Shippert, P. D. Brown, S. A. Clough, R. O. Knuteson, H. E. Revercomb, and W. L. Smith, 1998: Long-Term Analysis of Observed and Line-by-Line Calculations of Longwave Surface Spectral Radiance and the Effect of Scaling the Water Vapor Profile. *Proc. 8th Atmospheric Radiation Measurement (ARM) Science Team Meeting*, Tucson, AZ, U.S. Department of Energy, 773-776.

Turner, D. D., S. A. Clough, J. C. Liljegren, E. E. Clouthiaux, K. Cady-Pereira, and K. L. Gaustad, 2007: Retrieving liquid water path and precipitable water vapor from the Atmospheric Radiation Measurement (ARM) microwave radiometers, *IEEE Transactions on Geoscience and Remote Sensing*, **45**, 3680–3689.

van den Heever, S., G. L. Stephens, and N. B. Wood (2011), Aerosol Indirect Effects on Tropical Convection Characteristics Under Conditions of Radiative–Convective Equilibrium, *J. Atmos. Sci.*, **68**, 699–718.

Wagner, T. J., D. D. Turner, L. K. Berg, and S. K. Krueger, 2013: Ground-Based Remote Retrievals of Cumulus Entrainment Rates. *J. Atmos. Oceanic Technol.*, **30**, 1460–1471.

Wall, C., C. Liu, and E. Zipser, 2013: A Climatology of Tropical Congestus Using CloudSat, *J. Geophys. Res. Atmos.*, **118**, 6478– 6492.

Wang, S., 1993: Modeling Marine Boundary-Layer Clouds with a Two-Layer Model: A One-Dimensional Simulation. *J. Atmos. Sci.*, **50**, 4001–4021.

Williams, K. D. and G. Tselioudis, 2007: GCM Intercomparison of Global Cloud Regimes: Present-Day Evaluation and Climate Change Response. *Clim. Dyn.,* **29**, 231-250.

Xu, K.-M. and K. A. Emmanuel, 1989: Is the Tropical Atmosphere Conditionally Unstable? *Mon. Wea. Rev.,* **117**, 1471-1479.

Yano, J.-I., 2014: Basic Convective Element: Bubble or Plume? A Historical Review. *Atmos. Chem. Phys.,* **14**, 7019–7030.

Zhang, Y. and S. A. Klein, 2013: Factors Controlling the Vertical Extent of Fair-Weather Shallow Cumulus Clouds over Land: Investigation of Diurnal-Cycle Observations Collected at the ARM Southern Great Plains Site. *J. Atmos. Sci.,* **70**, 1297-1315.

Zhang, M. H. and J. L. Lin, 1997: Constrained Variational Analysis of Sounding Data Based on Column-Integrated Budgets of Mass, Heat, Moisture, and Momentum: Approach and Application to ARM Measurements. *J. Atmos. Sci.,* **54**, 1503–1524.